

AD-A079 679 AIR FORCE INST OF TECH WRIGHT-PATTERSON AFB OH SCH00--ETC F/6 20/5
SHOCK INDUCED STARTING OF GASDYNAMIC LASER NOZZLES. (U)
DEC 77 P A WEBER
JNCLASSIFIED AFIT/GAE/AA/79D-18

N1

1 OF 2

ADA
079870

LEVEL

(1)

SHOCK INDUCED STARTING OF
GASDYNAMIC LASER NOZZLES

THESIS

AFIT/GAE/AA/79D-18

Paul A. Weber
Capt USAF

1380

Approved for public release; distribution unlimited.

14

AFIT/GAE/AA/79D-18

12

103

6

SHOCK INDUCED STARTING OF
GASDYNAMIC LASER NOZZLES.

9

Master's THESIS

Presented to the Faculty of the School of Engineering
of the Air Force Institute of Technology
Air University
In Partial Fulfillment of the
Requirements for the Degree of
Master of Science

Allen

by

10

Paul ~~E~~ Weber
Capt USAF

Graduate Aerospace Engineering

11

December 1977

Approved for public release; distribution unlimited.

012 225

Gu

Preface

This investigation would have been impossible without the assistance and encouragement provided by my faculty advisory committee. The assistance provided by Dr. William C. Elrod was particularly crucial both to its completion and to the quality of the learning experience it represents. The time and effort contributed by technicians Mr. William W. Baker and Mr. H. Leroy Cannon were also substantial factors in reaching the intended goals.

Finally, the remarkable understanding and patience my wife and sons exhibited throughout the study was the true foundation upon which its success was built.

Capt Paul A. Weber

Contents

	<u>Page</u>
Preface.	ii
List of Figures.	v
List of Tables	vi
List of Symbols.	vii
Abstract	ix
I. Introduction	1
Background	1
Objective	3
Approach	3
II. Apparatus.	4
Shock Tube	4
Test Sections.	5
Electronics.	13
Time Delay Computer.	13
Standard Equipment	17
Flow Visualization	18
III. Results and Discussion	22
Summary.	22
Series 1	25
Series 4	32
Series 7 and 8	38
Series 10.	44
Size Effects	52
Theoretical Versus Actual Shock Tube Performance	53
Time Delay Computer Performance.	53
IV. Conclusions.	60
V. Recommendations.	62
Bibliography.	63
Appendix A: Nozzle Design Selection	65
Appendix B: Experimental Errors and Data Reduction.	68

	<u>Page</u>
Appendix C: Time Delay Computer Design and Operation	77
Appendix D: Silicon Controlled Rectifier Spark Lamp Trigger. .	83
Appendix E: Equipment Control Adjustments.	84
Appendix F: Schlieren Camera Alignment Procedure	86
Appendix G: Experimental Procedure.	88
Vita.	90

List of Figures

<u>Figure</u>		<u>Page</u>
1	Shock Tube System	6
2	Small Single Nozzle Profile	7
3	Single Nozzle Test Section Dimensions	8
4	Single Nozzle Test Section.	9
5	Multiple Nozzle Test Section (Internal Dimensions Only).	11
6	Multiple Nozzle Test Section.	12
7	Time Delay Computer Operation	16
8	Instrumentation Arrangement	19
9	Schlieren Camera Arrangement.	21
10	Flow Feature Nomenclature	26
11	Shock Tube Regions.	26
12	Test Series 1 Photographs ($t = 0$ at Throat)	27
13	Incident and Starting Shock Location versus Time in Series 1 and 4	33
14	Test Series 4 Photographs ($t = 0$ at Throat)	35
15	Test Series 8 Photographs ($t = 0$ at Throat)	39
16	Incident and Starting Shock Location versus Time in Series 7, 8, and 10.	42
17	Test Series 10 Photographs ($t = 0$ at Throat	45
18	Time Delay Computer Consistency	58
C1	Time Delay Computer Schematic	78
C2	Sample Oscilloscope Traces (All 50 $\mu\text{sec}/\text{Div}$ Horizontal).	79
D1	Trigger Schematic	83

List of Tables

<u>Table</u>		<u>Page</u>
I	Test Summary.	23
II	Predicted Versus Actual Test Section Entrance Shock Speeds	53
III	Time Delay Computer Distance Errors	54

List of Symbols

Abs	≡	Absolute
C	≡	Gage Correction Factor
d	≡	Distance
d_1	≡	Shock Sensor Separation Distance, inches
d_2	≡	Distance Between Second Shock Sensor and Shock Location at the end of Computed Time Delay Interval, inches
d_{2e}	≡	Expected Distance from Shock Sensor C to Shock in Photograph, inches
d_{2m}	≡	Measured Distance from Shock Sensor C to Shock in Photograph, inches
d%	≡	Percent Error in Expected Versus Measured Shock Location in Photograph
$\Delta\%$	≡	Percent Error between Predicted and Measured Test Section Entrance Shock Speed
Δt_1	≡	Elapsed Time Between Shock Sensor Signals, microseconds
Δt_2	≡	Computed Time Delay Interval, microseconds
f_1	≡	Time Delay Computer Fixed Oscillator Operating Frequency, Hertz
f_2	≡	Time Delay Computer Variable Oscillator Operating Frequency, Hertz
γ	≡	Ratio of Specific Heat at Constant Pressure to Specific Heat at Constant Volume
Hg	≡	Mercury
$h_{1,r}$	≡	Measured Mercury Manometer Column Height, inches
IC	≡	Integrated Circuit
M_s	≡	Shock Wave Propagation Mach Number
\bar{M}_{se}	≡	Average Test Section Entrance Shock Mach Number based on Δt_2
\bar{M}_{s1}	≡	Average Test Section Entrance Shock Mach Number based on Δt_1
M_{61}	≡	Predicted Shock Mach Number at Test Section Entrance

P_A \equiv Ambient Pressure, inches of mercury
 P_i \equiv Indicated Shock Tube Driver Section Pressure, inches of mercury
 P_1 \equiv Shock Tube Driven Section Pressure, inches of mercury
 P_4 \equiv Shock Tube Driver Section Pressure, inches of mercury
 P_{41} \equiv Shock Tube Diaphragm Pressure Ratio = P_4/P_1
 \bar{P}_{41} \equiv Average True (Corrected) Diaphragm Pressure Ratio
 t \equiv Time, seconds
 u_s \equiv Shock Wave Propagation Velocity (Laboratory Reference Frame), ft/sec
 \bar{u}_s \equiv Average Test Section Entrance Shock Propagation Velocity based on Δt_1 , ft/sec
 u_{61} \equiv Predicted Test Section Entrance Shock Speed, ft/sec
 w_c \equiv Gage Correction Factor Uncertainty
 w_d \equiv Shock Location Uncertainty, inches
 w_{d1} \equiv Uncertainty in Shock Sensor Separation Distance Measurement, inches
 w_{d2} \equiv Uncertainty in Shock Location Measurement from Photograph, inches
 w_{f1} \equiv Uncertainty in Time Delay Computer Fixed Oscillator Frequency Measurement, Hertz
 w_{f2} \equiv Uncertainty in Time Delay Computer Variable Oscillator Frequency Measurement, Hertz
 w_M \equiv Measured Mach Number Uncertainty
 w_n \equiv Measurement Uncertainty in Independent Quantity x_n
 w_{P_A} \equiv Ambient Pressure Measurement Uncertainty, inches of mercury
 w_{P_i} \equiv Indicated Driver Section Pressure Measurement Uncertainty, inches of mercury
 $w_{P_{41}}$ \equiv Measurement Uncertainty in Diaphragm Pressure Ratio
 w_t \equiv Time Measurement Uncertainty, seconds
 w_T \equiv Ambient Temperature Measurement Uncertainty, degrees Rankine
 w_u \equiv Shock Propagation Speed Measurement Uncertainty, ft/sec
 w_Z \equiv Uncertainty in Arbitrary Dependent Quantity Z
 x_n \equiv Arbitrary Set of Measured Quantities
 Z \equiv Arbitrary Dependent Quantity

Abstract

Dynamic processes occurring in single and multiple arrays of contoured Mach 3.2 rapid expansion, two-dimensional, supersonic nozzles during the passage of strong shock waves were investigated. Two sizes of single throat nozzles were tested. Their throat openings were 0.276 and 0.069 inch. The multiple nozzle array used had nine parallel nozzles of the smaller size arranged to simulate the flow channel of a gasdynamic laser. Several series of schlieren photographs were taken of the flow field within the nozzles. A fully started condition evidenced by uniform supersonic flow was observed in the small single nozzle and the multiple throat array approximately 80 microseconds after the passage of Mach 2.33 shock waves. The large single nozzle was not fully started by Mach 3.0 incident shocks. The dynamic flow initiation process was found to be strongly influenced by the strength and frequency of transverse wave reflections in the nozzle inlets. The large single nozzle's failure to start is believed to be due to the fact that its larger inlet size reduced the frequency of these reflections by an amount which prevented the rapid increase in effective reservoir pressure necessary for supersonic flow initiation.

A novel digital time delay computer was designed and built to facilitate making closely spaced photographs of the flow patterns. This device makes shock location in each photograph independent of the shock wave speed.

SHOCK INDUCED STARTING OF GASDYNAMIC LASER NOZZLES

I. Introduction

Background

A gasdynamic laser (GDL) is a device in which a series of supersonic nozzles is employed to generate a region in the flowing media having a population of low temperature, high energy molecules suitable for lasing action. The flow channel is usually configured as a linear array of two-dimensional, convergent-divergent supersonic nozzles immediately followed by a cavity in which the lasing action takes place. The output beam emerges from the cavity in a direction perpendicular to the nozzle contours and is directed by external optical components.

GDLs and the physical processes upon which their operation depends have been the subjects of intense investigation in a quest for greater beam power and increased operating efficiencies. One aspect of a GDL's overall efficiency is the quantity of fuel consumed during the start-up process. In some applications where the available fuel supply is limited, the fraction which must be expended to establish operating conditions in the flow channel may adversely affect the installation's ability to perform its required task. An accelerated starting process would be highly advantageous in such situations. However, the operational design constraints of GDL flow channels create difficulties with techniques commonly applied to devices such as wind tunnels: nozzle geometry changes and adjustable diffuser areas. A solution involving only adjustments to initial flow

dynamics is, therefore, desirable.

Shapiro (Ref 1:139), Leipmann and Roshko (Ref 2:127), and many other authors describe the "steady-state" supersonic nozzle starting process in terms of (1) an increase in inlet pressure and/or decrease in exit pressure until (2) uniformly subsonic flow in the nozzle is followed by (3) sonic conditions at the throat and the formation of a normal shock which (4) moves downstream until it is expelled from the exit. This process may be considered steady-state in that until sonic conditions are achieved at the throat, flow throughout the nozzle is essentially uniform and, if at any time in the process the pressure ratio from inlet to exit is made constant, flow within the nozzle will persist in a form dictated by that pressure ratio. This is the process with which GDL nozzles and cavities are usually started. Of course, the time span over which the process takes place may be relatively short, but the flow channel and associated plumbing are optimized for continuous flow.

As a result of interest in using shock tube apparatus as an inexpensive way of achieving very high velocity gas flows, Smith (Ref 3), Amann (Ref 4), and others have examined the use of convergent-divergent, reflection-type nozzles as a means of overcoming inherent shock tube limitations. The results of such investigations and the general similarity of a GDL flow channel to a shock tube wind tunnel indicate that a strong shock wave propagating through the channel may product the desired rapid flow initiation. However, their studies and those of Gvozdeva, et al. (Ref 5) were limited to single nozzles with straight taper diverging sections. Others, for example, Leverance, et al. (Ref 6), have used shock tubes to investigate GDL nozzle and cavity flow, but they examined the flow after start-up was complete.

Objective

The objective of this experimental study was to photographically examine the highly dynamic processes taking place during the passage of strong shock waves through contoured, convergent-divergent, two-dimensional nozzles simulating those found in gasdynamic lasers.

Approach

Tests were conducted in the Air Force Institute of Technology 4 inch by 8 inch by 20 foot shock tube with ambient temperature air as both driver and driven gas. Basic shock tube performance was analyzed according to the classical methods given by Leipmann and Roshko (Ref 2: 79-83).

Two test sections and three nozzle configurations were investigated at shock tube diaphragm pressure ratios of 5, 13, 28, 37, and 64. Corresponding test section entrance shock Mach numbers were approximately 1.6, 1.9, 2.2, 2.4, and 3.0. The nozzle used was an existing rapid expansion design optimized for $M = 3.2$ continuous flow. Two different sizes of a single-throat example of this nozzle were used in order to examine the effect of size on the transient phenomenon during flow initiation. The third configuration, a multiple nozzle assembly with nine throats, was used to examine inlet and exit phenomena unique to such arrays.

The primary data were photographs of the flow field within the nozzle assembly and in the region near the exit plane taken at known times. From the photography, flow quality in terms of turbulence and flow regime, and incident shock speed as a function of location was extracted.

II. Apparatus

Shock Tube

The investigation was conducted in the Air Force Institute of Technology 4 inch by 8 inch by 20 foot shock tube described by Egan and Foster (Ref 7). The shock tube's 16-foot-long driven end pressure can be reduced below ambient by means of a Heraeus type E-70 vacuum pump and measured with a mercury manometer. Minimum attainable pressure was approximately 2.0 inches of mercury absolute.

The four-foot-long driver section of the shock tube is mounted on a combination longitudinal and lateral slide arrangement so that it may be moved for cleaning and diaphragm installation. It is locked to the driven section with the diaphragm between by means of a hydraulic cylinder actuated latch. Filtered compressed air from the laboratory supply was used to pressurize the driver section, and a Bourdon tube type gage calibrated from 0 to 200 inches of mercury measured the resulting pressure. Maximum available pressure was approximately 204 inches of mercury.

Type A Mylar sheet, ranging from 0.003 to 0.007 inches thick, was used for diaphragm material. About 0.06 mils of diaphragm thickness were required per inch of mercury pressure differential across the diaphragm. As many as four sheets of material were used. A pneumatic plunger with a sharpened pyramidal tip ruptured the diaphragm on command.

In order to increase the strength of the shock entering the test section, a straight-taper area reducer was mounted in the downstream end

of the main shock tube. It reduces the 8-inch dimension to 5 inches over a distance of 2 feet, and the 4-inch dimension to 1 inch over a distance of 1 foot. A 4-foot-long, 1 inch by 4.5 inch, rectangular cross-section chamber was mounted on the end of the main shock tube so that the strengthened shock could stabilize after the area reduction. All test sections were attached to its downstream end with suitable adaptor plates.

Shock tube operating controls are diagrammed in Fig 1. They consist of two basic circuits: (1) driver end pressurization (P_4) and measurement, and (2) driven end evacuation (P_1) and measurement. The arrangement permits isolation of the P_4 gage and P_1 manometer from the shock tube to prevent damage by the shock wave.

Test Sections

Two test sections were used. They permitted mounting two sizes of a Mach 3.2, single-throat, two-dimensional, convergent-divergent, supersonic nozzle. Figure 2 is a drawing that describes the profile of the smaller of the two sizes in terms of x and y coordinates. The larger size profile was exactly four times the given dimensions; the throat opening was 0.276 inch and the expansion section length was 2.936 inches. The rationale behind selection of this particular profile is contained in Appendix A.

The first of the two test sections permitted mounting upper and lower sidewalls contoured to produce large or small single-throat examples of the nozzle. Figure 3 gives key dimensions of these assemblies and Fig 4 contains photographs of both with one of the window-containing lateral sidewalls removed. The inlet adaptor plate and the downstream end cap have also been removed for clarity.

The second test section contained eight complete nozzle blades and

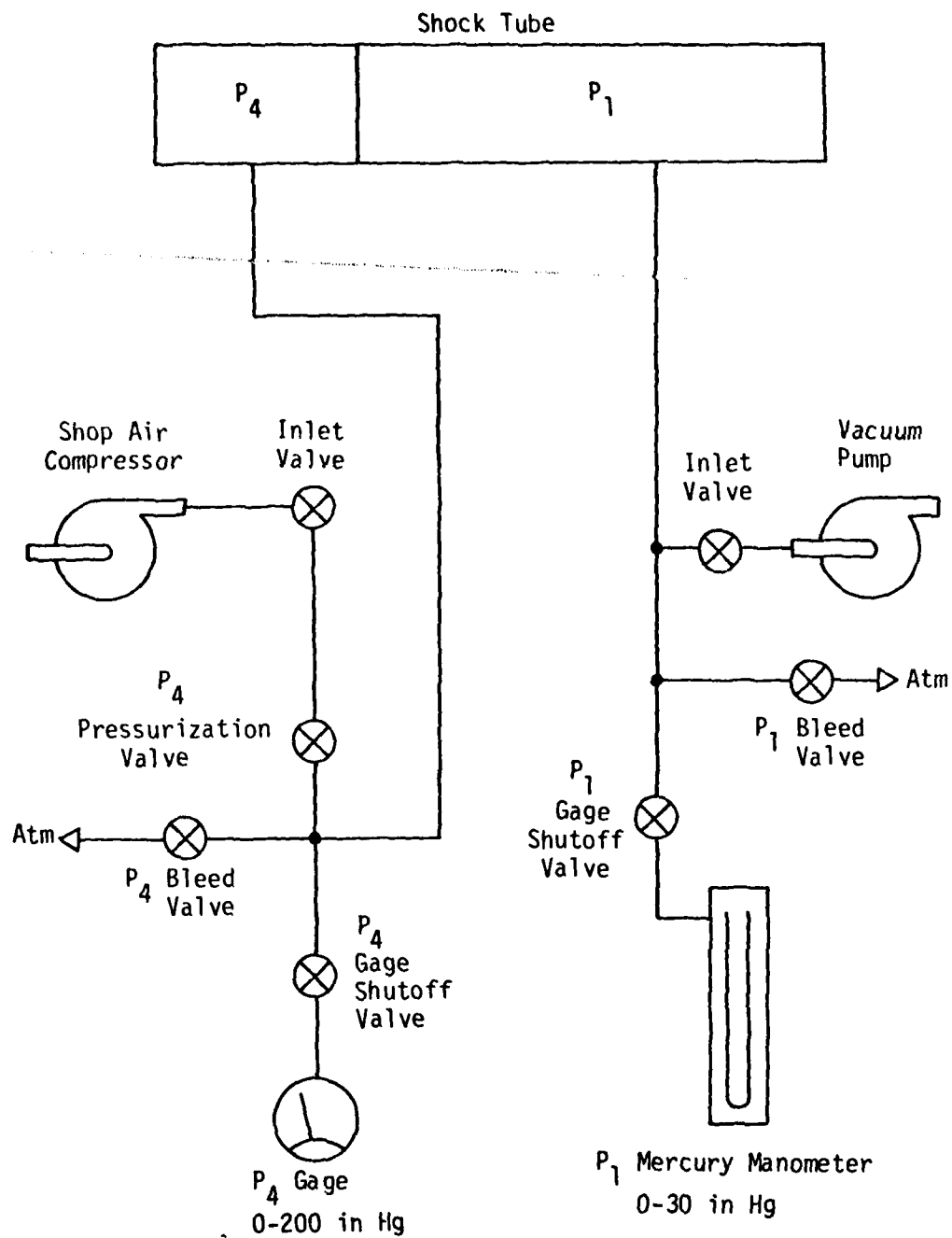


Fig 1. Shock Tube System



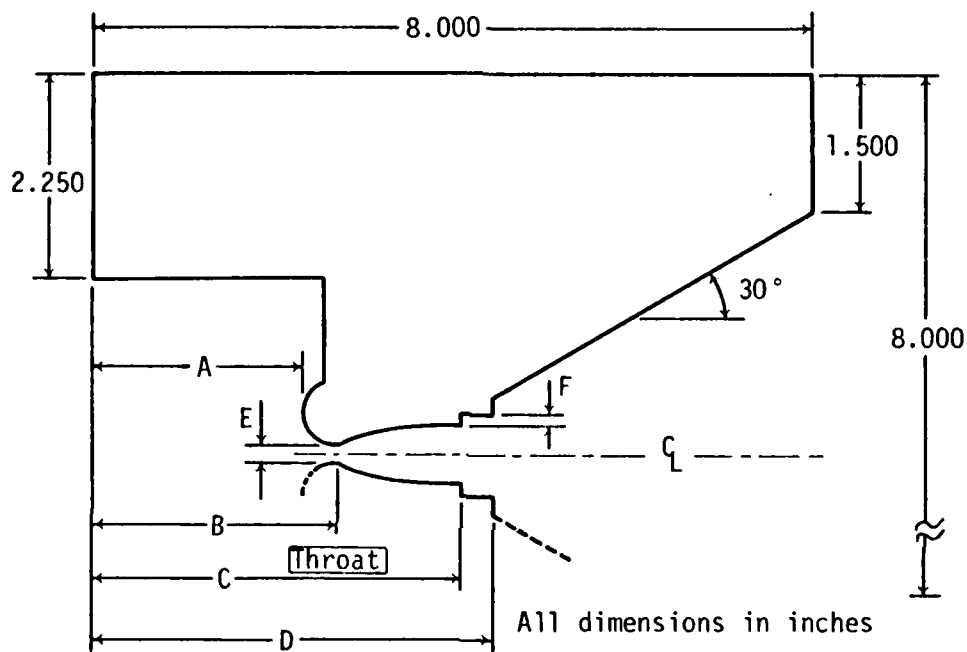
All Dimensions in Inches

X	Y	X	Y	X	Y	X	Y
0.0	0.168	0.133	0.106	0.250	0.071	0.446	0.037
0.044	0.146	0.146	0.101	0.272	0.066	0.485	0.033
0.069	0.132	0.161	0.096	0.295	0.061	0.526	0.030
0.083	0.127	0.176	0.091	0.321	0.056	0.572	0.026
0.095	0.121	0.193	0.086	0.349	0.051	0.621	0.024
0.107	0.116	0.210	0.081	0.378	0.046	0.675	0.022
0.120	0.111	0.229	0.076	0.411	0.042	0.734	0.021

Throat Opening = 0.069 inch
 Total Length = 0.902 inch
 Design Mach = 3.23

Large Single Nozzle is 4 times all dimensions.

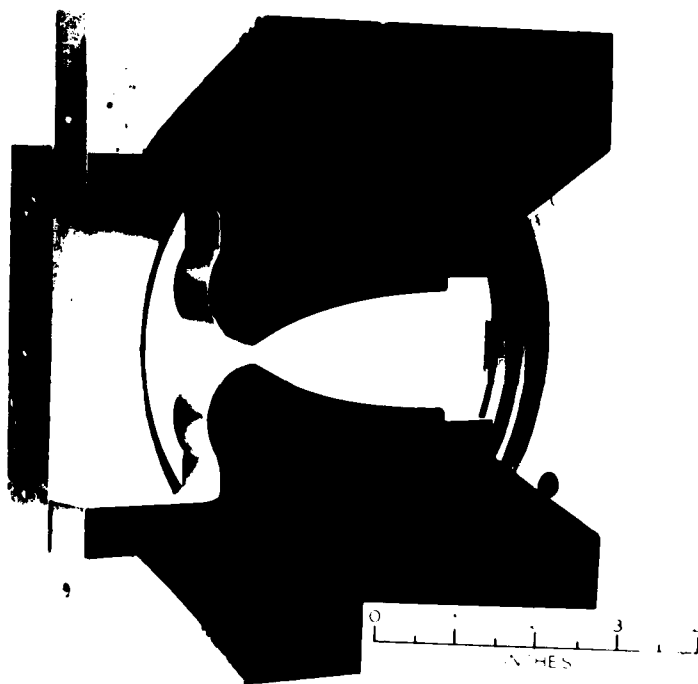
Fig 2. Small Single Nozzle Profile



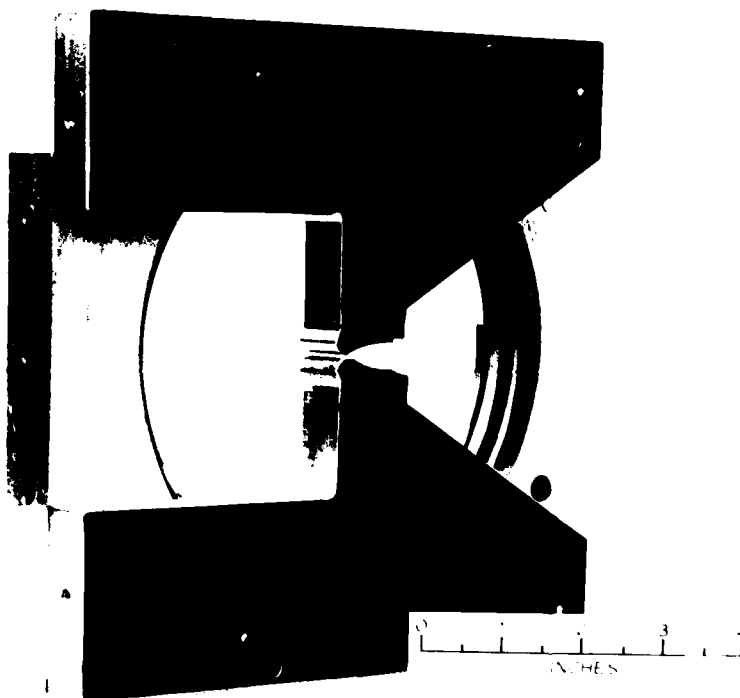
Material : 0.750 Thick Aluminum

Dimension	Large Nozzle Test Section	Small Nozzle Test Section
A	1.678	3.632
B	2.350	3.800
C	5.286	4.534
D	6.070	4.730
E	0.276	0.069
F	0.084	0.021
Throat To Sensor C	8.651	10.101

Fig 3. Single Nozzle Test Section Dimensions



(A) Large Nozzle



(B) Small Nozzle

Fig 4. Single Nozzle Test Section

two half-blades arranged to provide nine throats identical in size to the smaller of the single nozzle arrangements. Figure 5 is a drawing giving key dimensions of the multiple nozzle test section, and Fig 6 portrays it in two stages of assembly.

Both single nozzle profiles were constructed of aluminum alloy as was the remainder of the assembly. Both used the same optical glass windows. The windows had been abraded by contaminants in the gas during previous use in continuous flow studies leaving a visible pattern of pits. The windows were rotated such that the pattern was at 90 degrees to the flow direction in the present study to minimize their visibility.

The multiple nozzle test section consisted of an aluminum alloy case surrounding plexiglas windows that were drilled to mount the nozzle blades with screws and pins. The windows in this assembly had also been pitted during previous studies, but no reorientation was possible.

Neither of the test sections' inlet dimensions match the stabilization chamber dimensions exactly. Both were 0.75 inch thick, 3.75 inches wide (single nozzle), and 3.64 inches wide (multiple nozzle) versus the stabilization chamber's 1.0 by 4.5 inches measurement. This area reduction did affect flow characteristics and will be described later.

Both test sections had provisions for installation of diffusers downstream of the throats. In the case of the single nozzle assembly, the diffuser was a 10 degree half-angle wedge that could be adjusted to any location from touching the throat to outside the exit plane. The multi-nozzle test section's diffuser blades were not adjustable, but could be removed individually. Figure 5 shows their location and dimensions. A few tests were conducted with the diffusers in the visible flow field in order to obtain downstream flow velocities by measuring oblique

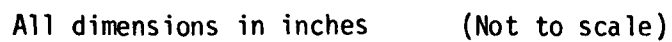
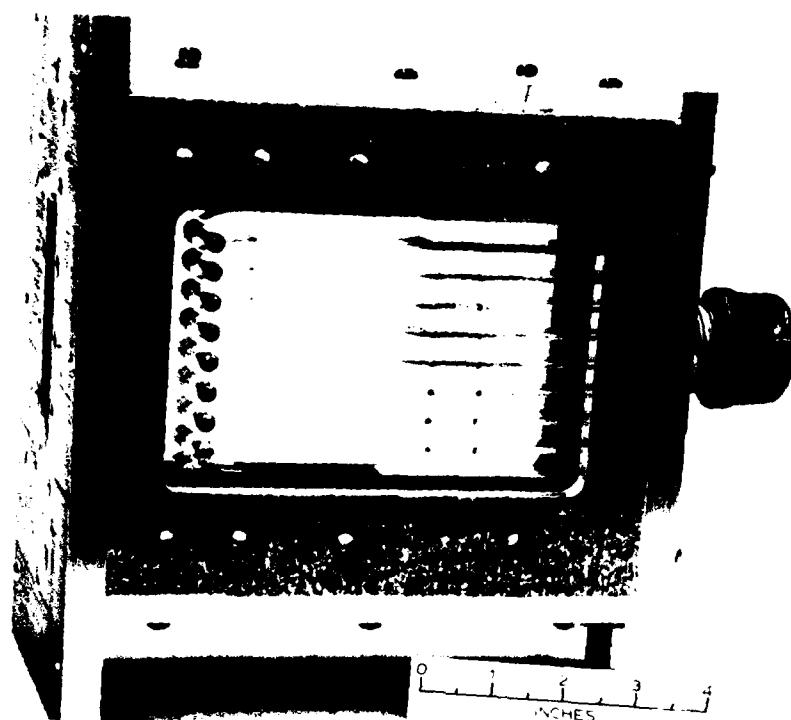
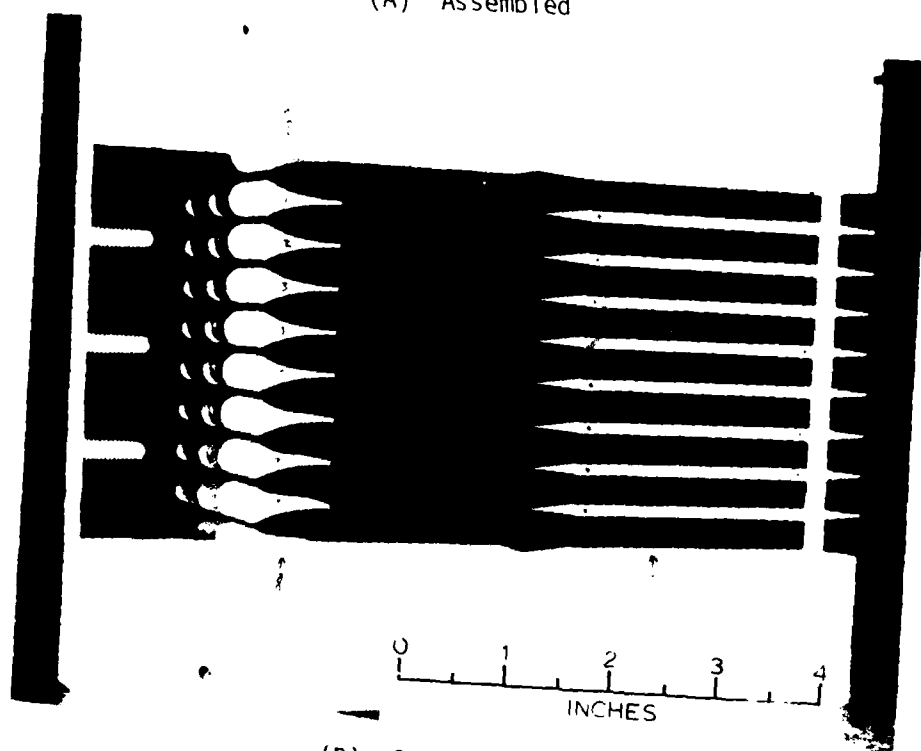


**Fig 5. Multiple Nozzle Test Section
(Internal Dimensions Only)**



(A) Assembled



(B) Small Nozzle

Fig 6. Multiple Nozzle Test Section

shock locations and angles.

Electronics

An assembly of electronic equipment was used to detect the presence of the shock wave, to measure its velocity, and to generate an appropriately timed signal to discharge a high-intensity spark lamp for photographing the resulting flow patterns. A unique digital time delay computer was designed to generate the timing signals. Because this device may prove of great value in the conduct of other types of tests involving rapid transient events, it will be described separately from the conventional equipment used.

Time Delay Computer. Whenever a rapid transient event must be captured by means of photography, X-ray imagery, or similar one-shot, time-sensitive recording devices, there is always a problem in determining exactly when the recording device should be operated to ensure that the object of study is within the recorder's field of view. Obviously, some instrument sensitive to the object of study's presence might be placed within the recorder's field of view and caused to "instantaneously" trigger it, but this is often impractical due to interference between the detector and the recorder. Therefore, the detector is usually placed outside the recorder's field of view, arranged so that a delay is introduced between the detector's signal and the recorder's operation. It is this arrangement that leads to the timing problem.

In the case of this study, the object of interest is a shock wave propagating through a duct and the recorder is a camera. Standard practice has been to place a shock detector (temperature, pressure, or density) a known distance upstream from the camera and connect it to an electronic

device capable of triggering the camera (or light source) a fixed interval of time after receiving the detector's signal. Successful operation of such a system depends on two factors: (A) the shock wave's velocity must be known in advance, and (B) the velocity must remain unchanged after the wave has passed the detector. Factor B is controlled largely by how "close" the detector is to the camera in terms of conditions which might change the shock speed (distance, area changes, obstructions, etc.). Given reasonably constant conditions between detector and camera, it is then Factor A which determines the accuracy with which the shock's location in the photograph may be determined in advance.

A common procedure is to estimate the shock speed which should result from the given operating conditions in the shock tube, calculate the time required for a shock traveling at this estimated speed to pass from the detector to the camera, set the delay generator to this figure, and conduct the test. Any deviation in shock speed from the estimate will result in a (linearly) proportional deviation of shock location in the photograph from that expected based on the estimated velocity. If the experiment demands photography at a precise shock position or with the shock at a series of closely spaced locations, it may be necessary to conduct a very large number of tests, or to employ more elaborate equipment, to obtain the required photographs. This is the problem addressed by the time delay computer.

The basic operating principle of the time delay computer is that it first measures the speed of the shock wave as it passes two detectors and then produces an output signal after a period of time inversely proportional to the speed of the shock, but directly proportional to the predetermined location at which the shock is to be for the photograph.

This effectively makes the shock's location when it is photographed independent of its speed.

Figure 7 shows the operating principle diagrammatically. When the shock passes the first of two sensors located upstream from the camera, the resulting electrical signal causes the computer's internal decade up/down counters to begin counting the frequency f_1 "up clock" pulses. When the shock passes the second sensor, the up clock is disconnected from the counters and the "down clock", a variable frequency oscillator operating at frequency f_2 , is connected in such a way that each of its pulses is subtracted from the number of up clock pulses that had just been counted. The time interval required for the shock to pass from the first sensor to the second is Δt_1 . A delayed output signal is then produced when the counters reach zero, by which time an interval Δt_2 has passed.

From Fig 7, the distance/time relationships are:

$$u_s = \frac{d_1}{\Delta t_1}$$

$$d_2 = u_s \Delta t_2 = \frac{d_1}{\Delta t_1} \Delta t_2 = \frac{\Delta t_2}{\Delta t_1} d_1$$

But, also note:

$$\frac{\Delta t_2}{\Delta t_1} = \frac{f_1}{f_2}$$

Therefore:

$$d_2 = \frac{f_1}{f_2} d_1 \quad (1)$$

Or:

$$f_2 = \frac{d_1}{d_2} f_1 \quad (2)$$

Thus, the desired location of the shock wave relative to the sensors at the time the output signal is generated is determined only by the

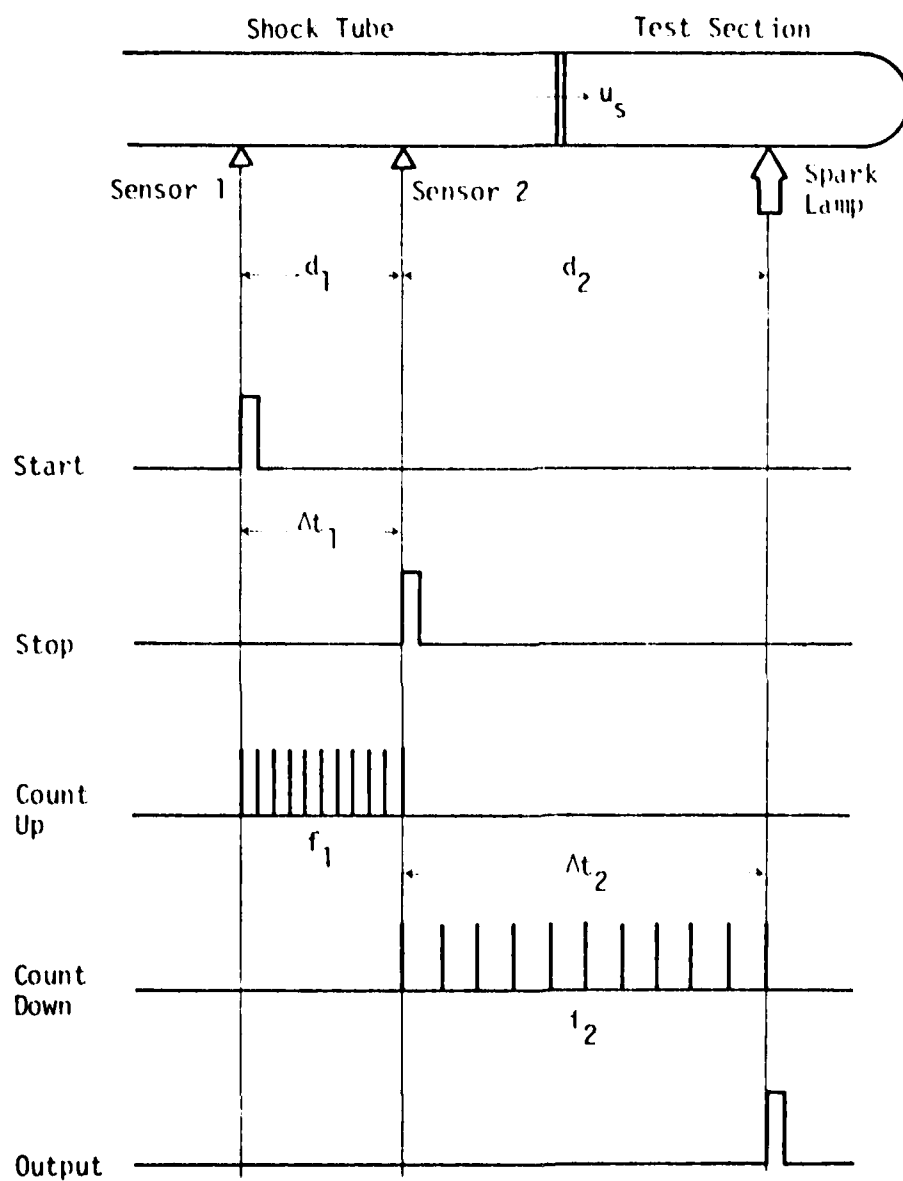


Fig 7. Time Delay Computer Operation

ratio of the clock frequencies and the distance between the two sensors, provided that the shock speed remains constant. Theoretical accuracy with which the shock may be located in advance is computed in Appendix B.

Appendix C contains a circuit diagram of the time delay computer as constructed in brassboard form for use in this study. It was implemented using standard TTL logic digital integrated circuits and other off-the-shelf components. Appendix C also contains a description of the circuit's operation and gives a parts list.

Two Computer Measurements Corporation model 726C digital counters were used to monitor delay computer clock frequencies f_1 and f_2 . A Wavetek model 186 function generator was the source of f_2 while an on-board, 10.000 MHz crystal oscillator provided f_1 .

The shock sensors were mounted 2.0 inches apart with the second 4.75 inches from the downstream end of the stabilization chamber. Thus, the 0 to 5 MHz range of the function generator used as the down clock permitted placing the shock at any downstream location up to as close as 4 inches (Eq 1) to the second sensor when the photograph was taken.

In operation, Eq 2 is used to compute the variable clock frequency necessary to yield a desired distance d_2 for the test. The down clock oscillator is set to this frequency as monitored by a digital counter and then the shock tube is fired.

Standard Equipment. Three Endveco model 2501-500 pressure sensors were mounted in the narrow sidewall of the stabilization chamber as shock detectors. The first, (denoted "A") was 8.75 inches upstream from the end of the section. The second (denoted "B") was 6.75 inches upstream, and the third (denoted "C") was 4.75 inches upstream. Sensor A was used only as an oscilloscope sweep trigger and otherwise played no part in

shock speed measurement or timing signal generation.

Each pressure sensor was connected to the input of an Electro Industries model A20B-1 variable gain instrumentation amplifier. Sensor A's amplifier was set for a gain of 10 for all tests and the output connected only to the external sweep trigger of a Tektronix model 549 storage oscilloscope. Usable amplifier gains for sensors B and C were found to be a function of the driven end pressure and varied from 10 to 100 during the course of the experiment.

Sensor B's amplified signal went to the channel 1 input of a Tektronix type M four channel plug-in unit installed in the oscilloscope and to the start input of the time delay computer. Sensor C's amplified signal was applied to the plug-in's channel 2 input and to the delay computer's stop input.

Delay computer outputs were connected as follows: the start channel pulse output was connected to the A input of a Hewlett-Packard model 5325B digital counter-timer and the stop channel pulse output was connected to the same timer's channel B input and also to the A input of a second identical timer. The computer's delayed output pulse was fed to a silicon controlled rectifier high voltage triggering circuit (described in Appendix D), the output of which was fed to a Cook Electric Model 596-4116 spark gap lamp.

Figure 8 shows the instrumentations connections diagrammatically; Appendix E lists the control settings on each piece of standard equipment used.

Flow Visualization

One photograph of the flow field within the test section was taken for each shot with a conventional single-pass Toepler-schlieren (Ref 8).

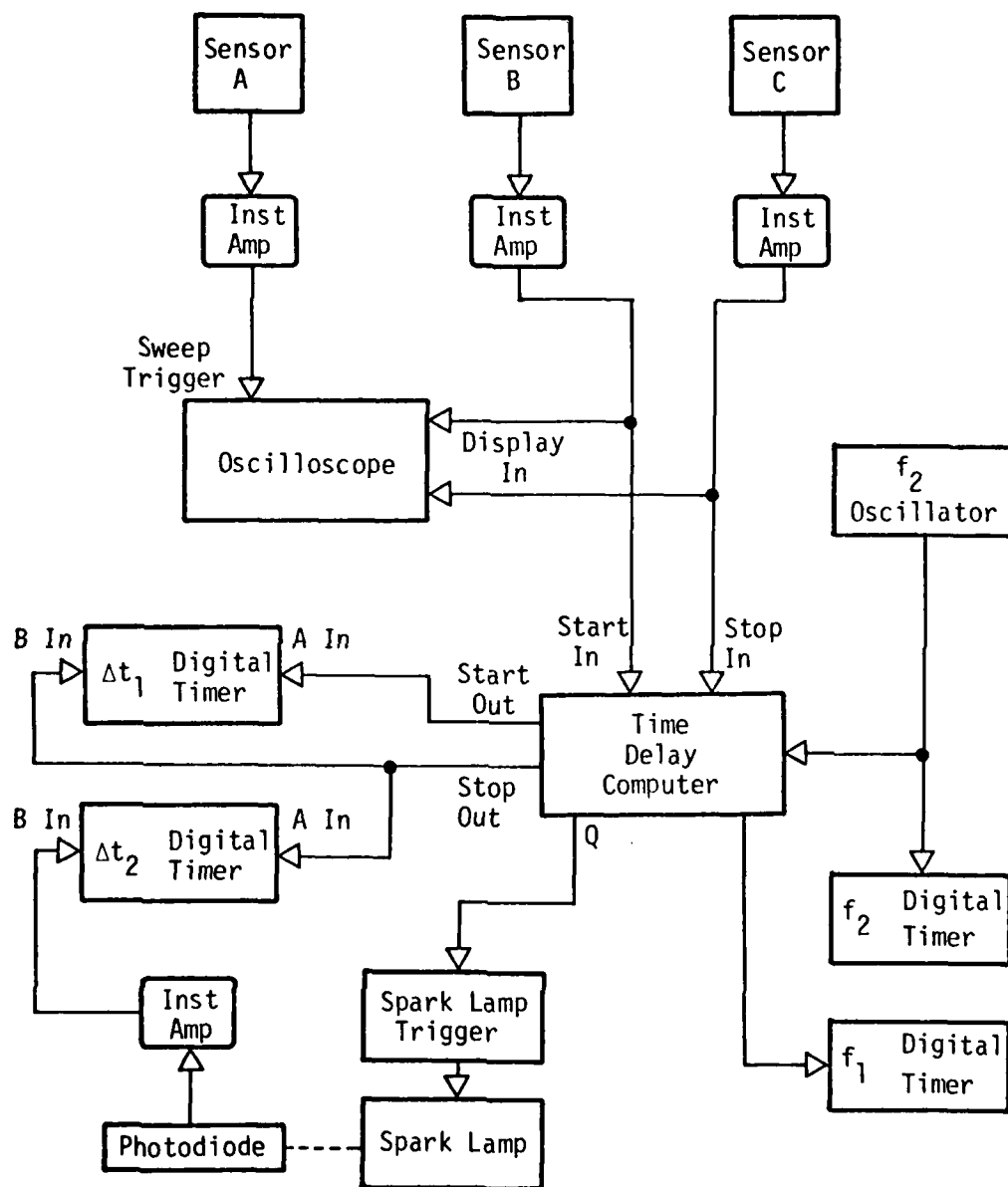


Fig 8. Instrumentation Arrangement

The equipment was arranged as diagrammed in Fig 9. It consisted of two 10-inch diameter, 30-inch focal length front surface parabolic mirrors, one plane front-surface mirror, an adjustable knife edge and a lensless camera equipped with an electrically operated shutter and a Polaroid model 100 film pack. The Cook Electric spark lamp mentioned above provided illumination consisting of a single 0.10 microsecond flash per test. An unbiased silicon photodiode placed in front of the spark lamp and connected through an amplifier to the B input of the second 5325B timer provided the signal indicating the point in time at which each photograph was actually taken. All flow field photographs were made initially on Polaroid type 107 film. A convenient alignment procedure for this equipment is described in Appendix F.

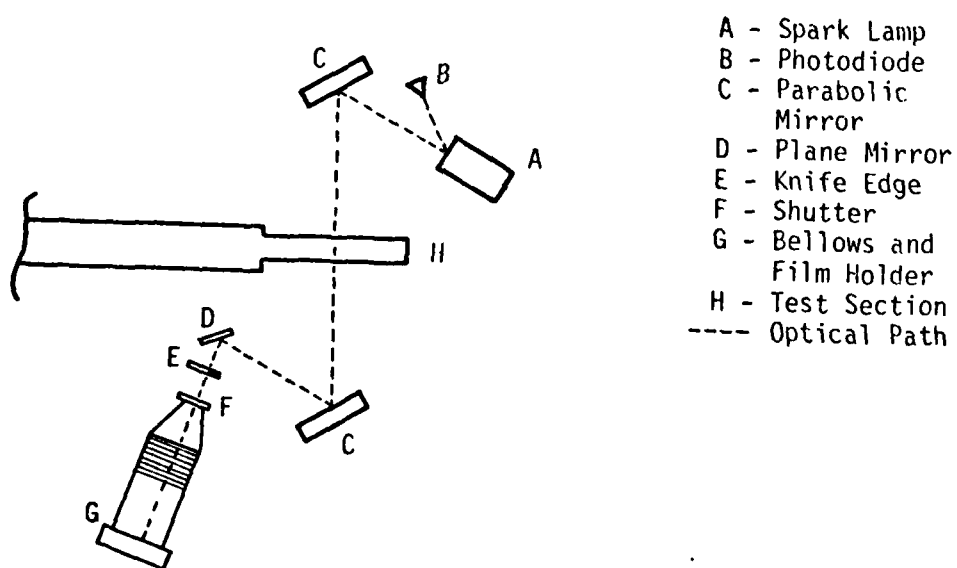


Fig 9. Schlieren Camera Arrangement

III. Results and Discussion

Summary

A total of 114 shock tube tests resulting in usable photographs were conducted. Fifty-one tests were conducted with the large single-nozzle test section, 15 tests with the small single-nozzle test section, and 48 with the multiple-nozzle test section. The tests were organized into 13 series, in each of which the incident shock strength, test section, or schlieren camera setup was different. Table I summarizes the test series: Appendix G summarizes the experimental procedure.

The first 6 test series were performed in the large single-nozzle test section at increasing shock tube diaphragm pressure ratios in order to verify instrumentation performance and provide a basis of comparison for small nozzle performance. Series 7 and 8 were conducted with the small single-nozzle test section using the highest shock tube diaphragm pressure ratio found to be repeatably attainable during the first group of tests. The schlieren camera was adjusted for an image magnification of approximately 2:1 for series 7; but the resulting photographs, while readable in the original, were too dark for reproduction due to the limited light output of the spark lamp.

Tests performed in series 9A through 9D were conducted in the multiple-nozzle test section with the diffuser blades visible in the photographs in order to determine flow velocity at their location. Series 9D was performed with the absolute maximum diaphragm pressure ratio attainable, which averaged 64.35 over the four shots in the series but were

TABLE I
Test Summary

Series	Test Section	Number Tests	\bar{P}_{41}	\bar{u}_s ft/sec	\bar{M}_{s1}
1	LSN	20	4.77	1758.95	1.56
2	LSN	6	12.93	2139.66	1.90
3	LSN	8	28.47	2503.07	2.22
4	LSN	8	37.50	2576.01	2.28
5	LSN*	6	36.78	2721.43	2.41
6	LSN*	3	36.07	2682.80	2.37
7	SSN	6	35.18	2633.00	2.33
8	SSN	9	36.07	2618.54	2.32
9A	MN*	4	36.07	2648.68	2.35
9B	MN*	5	35.91	2618.12	2.31
9C	MN*	5	35.85	2592.64	2.29
9D	MN*	4	64.35	3380.87	2.99
10	MN	30	35.90	2617.20	2.32

where:

Test Section Designations are: LSN \equiv Large Single Nozzle; SSN \equiv Small Single Nozzle; MN \equiv Multiple Nozzle

\bar{P}_{41} \equiv Average True Diaphragm Pressure Ratio

\bar{u}_s \equiv Stabilization Chamber (Test Section Entrance) Shock Speed, based on Δt_1

\bar{M}_{s1} \equiv Average Test Section Entrance Mach Number, based on Δt_1

*Diffuser(s) installed and visible in flow field

quite variable.

Test series 10 was performed in the multiple-nozzle test section with the camera adjusted for optimum coverage of the nozzle throats and approximately 2 inches of the downstream cavity. Thirty photographs were made at time intervals ranging from approximately 2 to 6 microseconds. These photographs, and those obtained in series 1 (as a weak-shock flow process comparison), series 4 (to observe scale effects), and in series 7 and 8 (as a means of identifying phenomena unique to multiple nozzle arrays), provided the bulk of the data collected. Data reduction procedures and a discussion of experimental uncertainties are in Appendix B.

In the discussion that follows, the term "test section" is applied to that part of the shock tube apparatus containing the three nozzle assemblies used and includes the adaptors with which the assemblies were mounted to the stabilization chamber section. Figures 3 and 5 show the exact extent of the test section region exclusive of the adaptor plates; their dimensions are discussed in Chapter II under "Test Sections."

A fully started nozzle condition was observed only in test series 7 through 10. The nozzle was judged to be fully started if the flow appeared uniformly supersonic throughout as indicated by the absence of visible shocks and by the presence of Mach lines originating from the contoured walls. Secondary evidence of a started condition was judged to be the presence of time-stable oblique shocks originating at the exit plane edges of the nozzle profile and extending downstream to form the classical Mach diamond pattern associated with over-expanded supersonic nozzle operation.

The only flow velocity determinations attempted in this investigation consisted of measurements of bow shock angles on test section diffusers

made in series 5, 6, and 9A-D. The results were judged unreliable because the shocks were both curved and detached. Velocity measurements based on Mach lines visible within the nozzle were considered inappropriate because of line curvature and the fact that true local flow direction at any point could only be approximated.

Test series 1, 4, 7, 8, and 10 are discussed in detail, followed by a discussion of actual versus predicted test conditions and time delay computer performance. The nomenclature which was applied to major flow features visible in the photographs presented in this section is shown schematically in Fig 10.

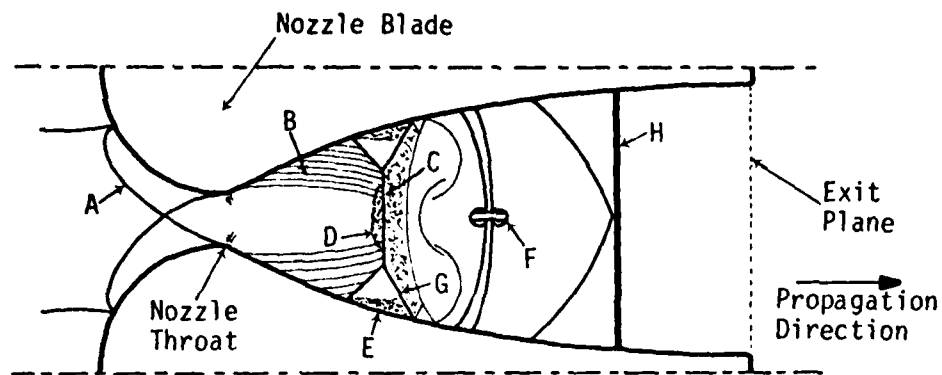
Series 1

The static pressure ratio P_{71} obtained in this series (see Fig 11 for region definitions) of 2.67 was much lower than the 51.7 required for continuous operation of a $M = 3.2$ nozzle. The nozzle was, therefore, not expected to fully start.

Figure 12A through L is a sequence of schlieren photographs taken during test series 1. Variations in flow field darkness from one photograph to the next are due primarily to variations in the exact point on the spark lamp electrode from which the light-producing discharge originated. These variations changed the effective location of the schlieren system knife-edge relative to the image path.

Figure 12A shows the appearance of the large single-nozzle test section before the incident shock's arrival. The throat and exit plane are identified in the figure as are visible flaws in the test section window glass.

In Fig 12B through D, the incident shock enters the field of view



- | | |
|---------------------------------|----------------------------|
| A - Transverse Inlet Reflection | E - Contour Boundary Layer |
| B - Mach Lines | F - Axial Jet |
| C - Starting Shock | G - λ Pattern |
| D - Boundary Layer Leakage | H - Incident Shock |

Fig 10. Flow Feature Nomenclature

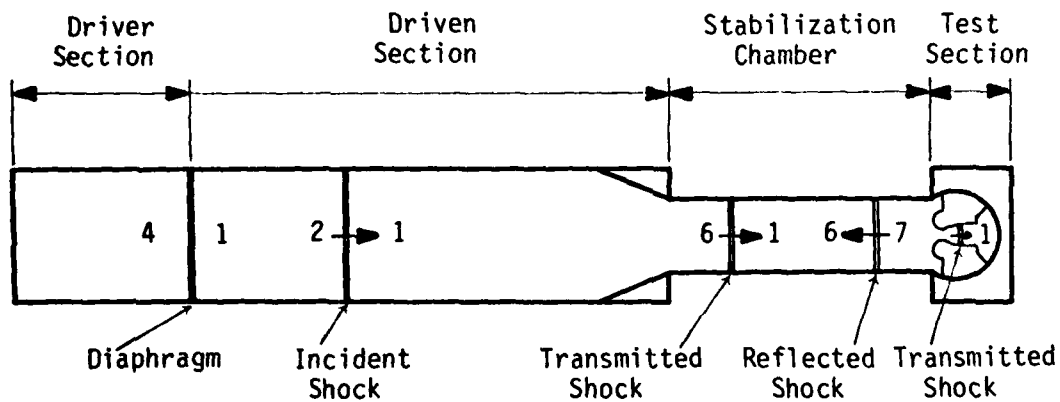
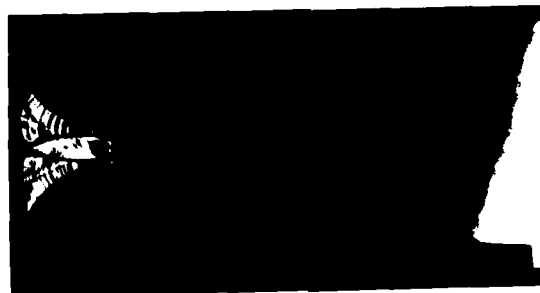
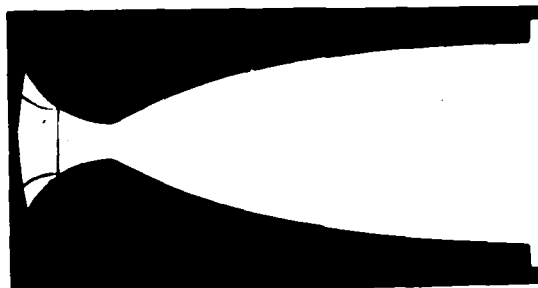
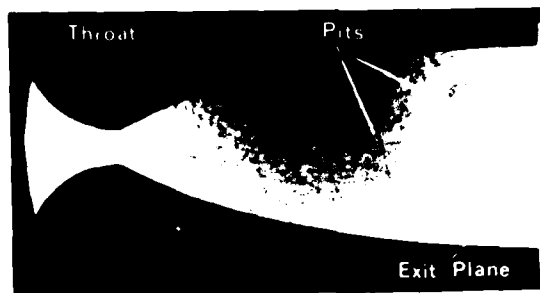
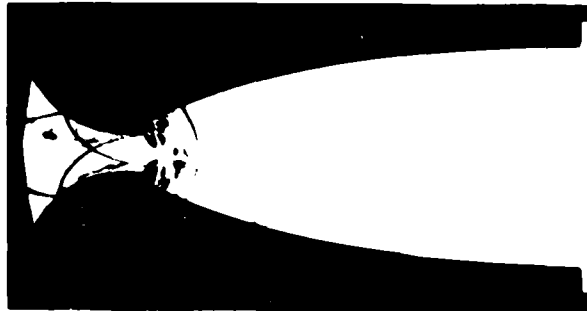


Fig 11. Shock Tube Regions







100.0 sec



103.7 sec



122.7 sec



130.7 sec

Fig. 1. a) front

and propagates toward the throat. Note the presence of strongly curved transverse reflections originating from the ends of the incident shock. An additional pair of transverse shocks is also present in these photographs and is most visible in B and C. Although they seem to be associated with the shocks reflected from the nozzle inlet, their relative location and comparative weakness makes it more likely that they are part of the reflection resulting from the incident shock's encounter with the area reduction between the stabilization chamber and the test section.

Figure 12D clearly shows a complex system of shocks and expansions behind the incident shock that originate from the inlet surfaces. The periodic nature of these features makes it likely that they are due to tool marks in the inlet surface.

Direct contact between the inlet reflection shocks and the incident shock has ceased by the time part E of Fig 12 was made. The downstream ends of the inlet reflections have separated from the upstream ends during their passage through the large pressure gradient existing at the throat. Between E and H the separated portions of the inlet reflections are seen to be reinforced by further separated sections of the inlet reflections. In H, it is obvious that a rapidly thickening turbulent boundary layer has formed and separated from the nozzle walls downstream from their intersection with this shock system.

The Mach "V" described by Amann as forming in the throat region has, meanwhile, progressed downstream and developed into a secondary or starting shock which may be compared to the starting shock observed during a "steady-state" startup process. The function of this starting shock is to adjust the static pressure from that existing in the uniform supersonic flow upstream to a condition compatible with the downstream pressure. This

shock is propagating upstream relative to the local flow, but the local flow is moving toward the exit with a greater velocity so that the resultant motion is away from the throat. The fact that the shock is concave toward the throat through part I indicates that the gas flow has a radially outward velocity component.

Subsequent to part I of Fig 12, the starting shock assumes an indistinct, ragged appearance for two reasons: (1) highly complex shock/expansion reflections are occurring downstream of the shock which produce a laterally unsteady pressure distribution behind it and lead to small-scale perturbations in its shape, and (2) because the starting shock has assumed a virtually fixed position relative to the nozzle, a separated turbulent boundary layer has had time to form on the test section windows at their intersection with the shock. As the window boundary layer grows thicker, the λ -pattern associated with the intersection also grows until it produces the appearance of turbulent flow "leaking" upstream past the starting shock. This evidence that flow in the region is no longer two-dimensional was also observed by Zhilin, et al., (Ref 9), although under slightly different conditions, and will be discussed in more detail later.

A "jet" has begun forming along the nozzle axis in the region of complex interactions between the incident and starting shocks in G and is fully developed in part H. Gvozdeva, et al. concluded that the jet results from the coalescence of transverse compression waves on the centerline. This appears possible, but the fact that it, and the pair of transverse waves with which it is associated, are quite stable in position from part H onward suggests that it may also represent a region in which high pressure between the two waves it pierces is relieved by a "blowout" to lower pressure areas up and downstream.

Fully developed supersonic flow from the throat at the starting shock is seen in part L of Fig 12. Mach lines originating on the expansion contour's wall form a pattern classically associated with such flow conditions. Note that these Mach lines are superimposed upon the boundary layer leakage around the starting shock described above.

Other than the stronger transverse inlet shocks produced by a larger inlet radius (2.4 times the throat opening versus 1.7 in Amann) and a more strongly curved shock pattern near the throat, test series 1 displays the same flow features observed by other investigators in nozzles with straight taper expansion sections. Another obvious (and expected) difference is the nozzle's failure to expel the starting shock.

Figure 13 is a plot of incident and starting shock locations relative to the nozzle throat versus time. Similar data from test series 4, to be discussed below, is plotted on the same scale. The data from both series plotted in Fig 13 have been shifted so that at time $t = 0$, the incident shock wave was at the throat. Not all photographs are represented by plotted points because of occasional failure of the digital counters used to measure Δt_1 and Δt_2 .

Series 4

Test series 4 is representative of large single nozzle experiments conducted at the highest shock tube diaphragm pressure ratio that could be repeatedly obtained--approximately 37. The resulting static pressure ratio $P_{71} = 5.9$ was still grossly insufficient for nozzle starting according to the isentropic steady-state theory of nozzle operation. Transverse inlet shock strengthening of the incident shock was expected to bring dynamic conditions behind the incident shock close to starting conditions.

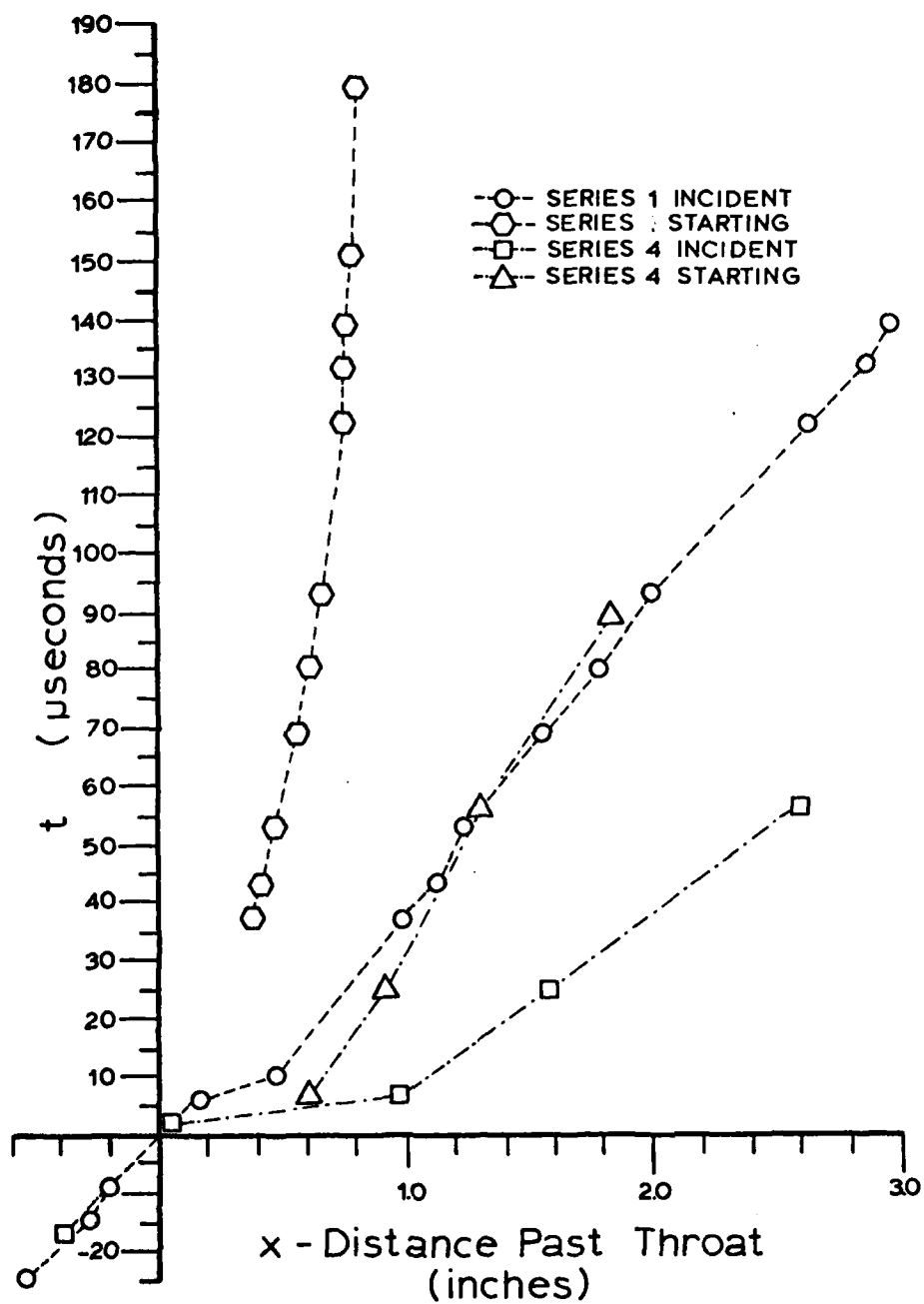


Fig 13. Incident and Starting Shock Location versus time in Series 1 and 4

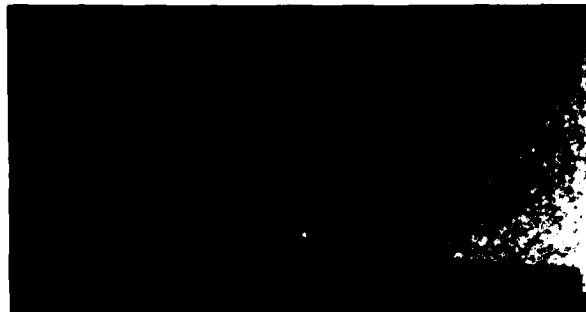
Figure 14A through H is a sequence of schlieren photographs from this test series. The incident shock shown in part A of this figure is in essentially the same location as in part B of Fig 12, but the second set of transverse reflected shocks present in the series 1 photograph is not visible.

Flow features visible in part B of Fig 14 are quite similar to those in the corresponding incident shock location in test series 1. From C onward, however, there are significant differences. The curvature of the inlet profile reflected shocks is distinctly decreased through their intersection with the pattern of fine compression waves originating on the inlet surface. Further, this pattern of fine waves appears less strongly curved near the throat than was the case in series 1.

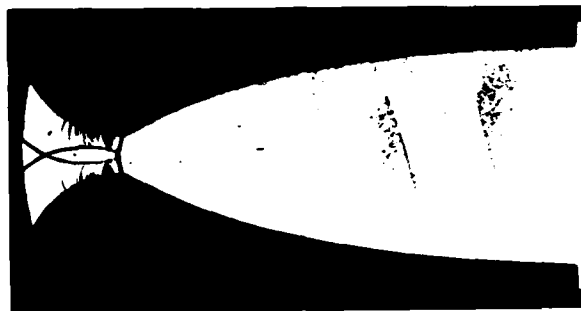
A more significant difference between the weak incident shock results in series 1 and this series is that between part C and D of Fig 14, the nozzle starting shock has started to form without the formation of a Mach "V" in the intersection of the transverse inlet shocks. The starting shock is also seen to be much more strongly concave toward the throat in part E even though the rapidly thickening turbulent boundary layer along the profile wall is present and roughly the same size as in the earlier case.

Flow features in E are somewhat obscured by marks on the test section windows left by diaphragm debris. This was a serious problem throughout the experiment in that the test sections had to be removed and disassembled for cleaning after every four to five shots at the higher pressure ratios. It proved impossible to clean the shock tube thoroughly enough without test section removal to prevent such buildups on the windows.

Supersonic flow has developed in the region from the throat to the starting shock as shown in part F of Fig 14. The starting shock is noticeably



(A) $t = -16.5$ sec



(B) $t = -1.2$ sec



(C) $t = 2.6$ sec



(D) $t = 5.1$ sec

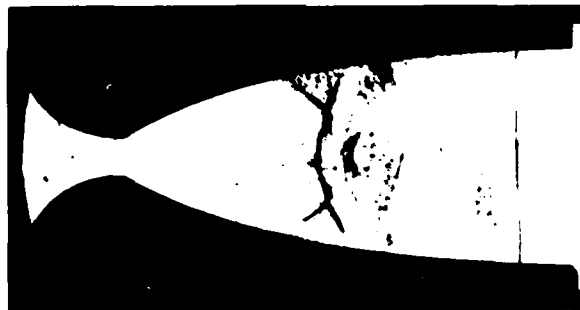
Fig 14. Test Series 4 Photograph
 (t = 0 at Throat)



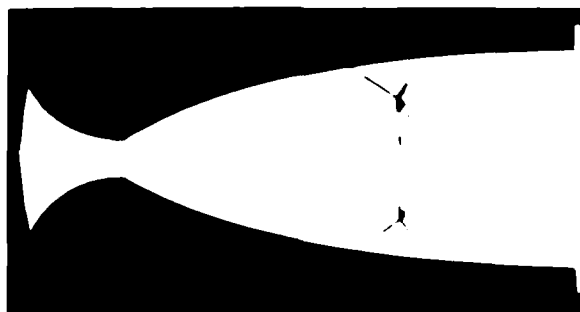
(E) $t = 7.6 \text{ .sec}$



(F) $t = 25.6 \text{ .sec}$



(G) $t = 56.6 \text{ .sec}$



(H) $t = 89.6 \text{ .sec}$

Fig 14. (Continued)

less concave toward the nozzle and the inlet reflected shock pattern is completely disassociated from it.

A distinct pattern of very fine periodic waves is seen to originate from the intersection of the incident shock and the nozzle walls in F and propagate upstream and toward the centerline. Similar features are very faint, but visible, in the series 1 photographs.

In part G of Fig 14, the starting shock has become concave toward the nozzle exit. Many of the flow features between it and the incident shock have dissipated by this time but the transverse inlet reflection process is still visible. Again, Mach lines originating on the nozzle walls between the starting shock and the throat indicate that this is a region of uniform supersonic flow.

A jet developing on the nozzle centerline is visible in parts E and F. It is much less distinct than the jet formed in series 1. The upstream-facing portion of the jet's mushroom shape is absent.

Figure 14H was the last photograph obtained in the series. The region of fully supersonic flow has increased in extent and the inlet reflections are no longer visible. The starting shock is again nearly normal and straight. Other photographs taken in test series 5 about 100 microseconds later show that the starting shock never progresses much further toward the exit plane under these test conditions. Instead, the turbulent window boundary layer grows thicker until the visible starting shock appears to be surrounded by turbulence and finally disappears. The plotted shock location versus time data in Fig 13 for this test series indicates a contrary trend for unknown reasons. Measurements based on oblique bow shock angle on the diffuser made in test series 5 give a very rough estimate of flow Mach number of 1.8 near the starting shock's

location in H.

This nozzle's failure to start under conditions which did yield starting in the small nozzle test sections is not yet fully understood. Proportional boundary layer thickness effects within the nozzle seem an unlikely explanation because such effects would tend to favor starting of larger nozzles rather than smaller ones.

Test series 4 shows that the dynamic processes in this nozzle differ in several respects from those observed in straight-taper expansion nozzles with smaller inlet radii. First, axial jets formed are characteristically single-sided. Second, the transverse inlet reflected shock pattern persists for a longer period. Third, the nozzle's throat or starting shock continues to develop during direct interactions between the inlet reflections and transverse wave reflections just behind the incident shock. These persistent reflections seem to play a major role in the observed processes.

Series 7 and 8

The only significant difference between series 7 and 8 is that the schlieren camera was adjusted for different image sizes in the film plane. The photographs from series 8 are presented as Fig 15A through H, and Fig 16 is a plot of incident and starting shock locations versus time for both series. As in Fig 13, zero on the time axis represents incident shock passage through the throat. Series 10 data is also plotted in Fig 16; it will be discussed later. The velocity of the shock wave incident on the test section was essentially the same in series 4, 7, 8, and 10.

Part A of Fig 15 depicts the small single-nozzle profile, nozzle block holders, incident shock, exit plane, and adjacent nozzle flow simulators. Recall that this nozzle is identical in form to the large single



(A) $t = -10.2 \text{ sec}$



(B) $t = -8.7 \text{ sec}$

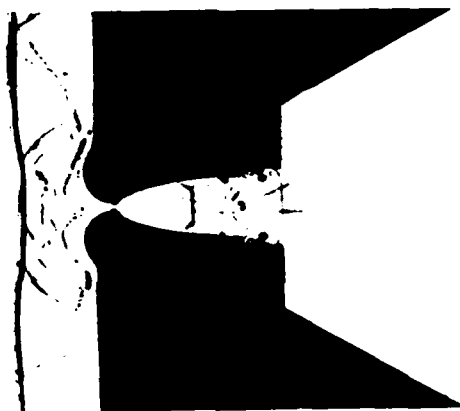


(C) $t = 5.3 \text{ sec}$

Fig 15. Test Series 8 Photographs
($t = 0$ at Throat)



(D) $t = 24.3$ sec



(E) $t = 30.3$ sec



(F) $t = 54.3$ sec

Fig 15. (Continued)

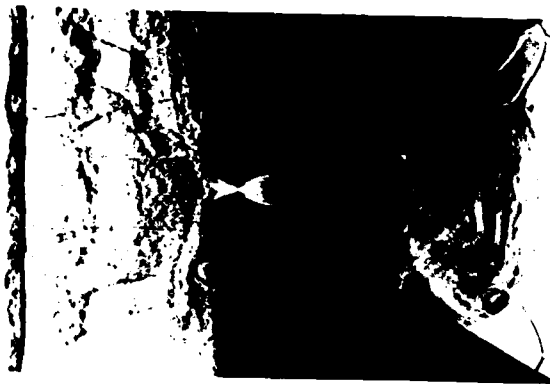


Fig. 15a



Fig. 15b

Fig. 15. (Continued)

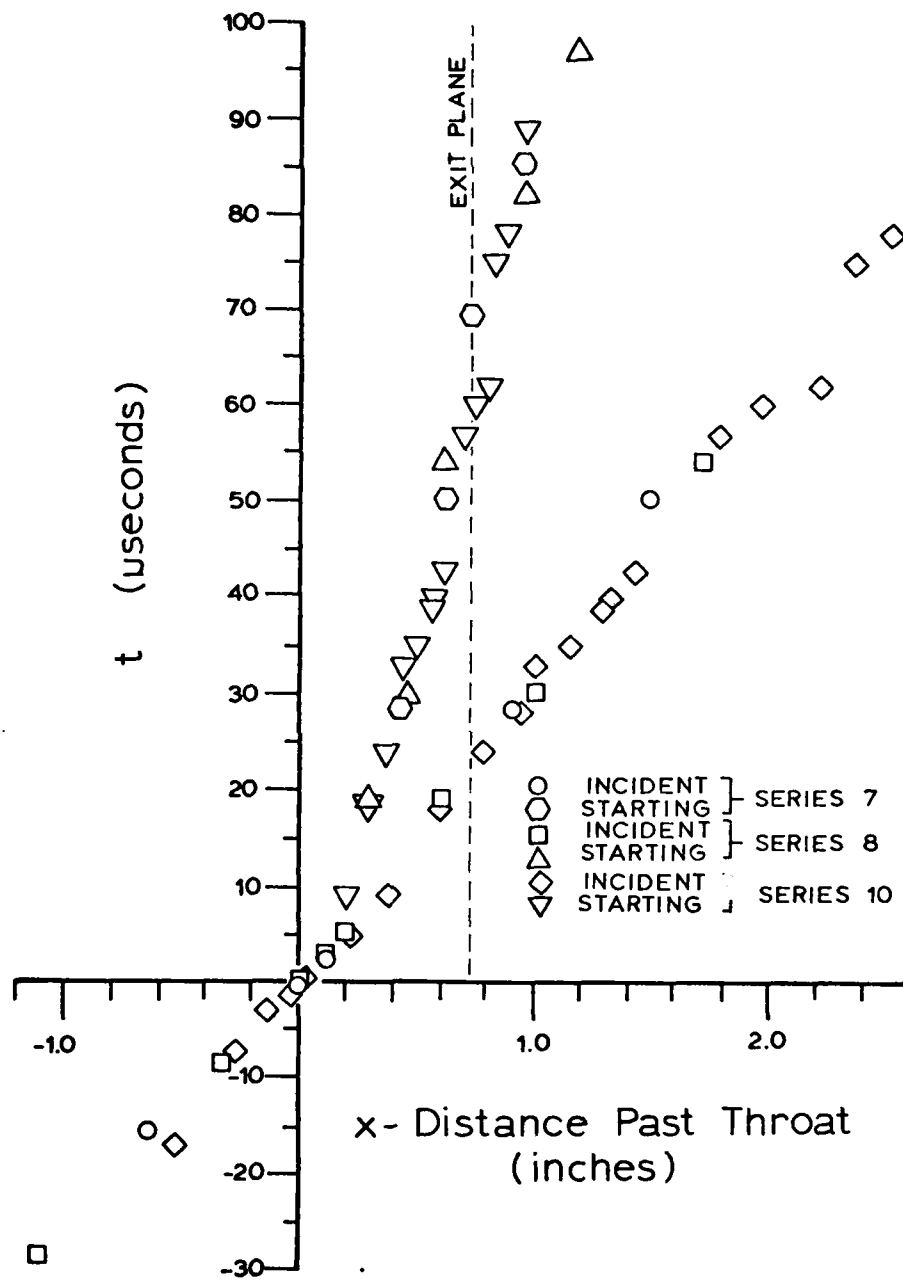


Fig 16. Incident and Starting Shock Location versus Time in Series 7, 8, and 10

nozzle tested in series 1 and 4, but is only one-fourth as large.

Transverse reflection waves behind the incident shock are visible in parts A through C of Fig 15. They are related to the shock's encounter with the test section entrance area reduction.

The normal shock reflection process from the nozzle blocks is clearly visible in part C. The same thickening of the reflected incident shock noted inside the nozzle in series 4 is evident here. A simplified explanation of the phenomenon follows: before the incident shock's passage, the gas in the test section entrance is stationary and after its passage it has a downstream velocity dependent upon the shock's strength. A boundary layer develops on the walls in which the velocity, according to viscous theory, must progress from zero at the wall to some freestream value outside the boundary layer. The reflected shock is thus propagating into a moving fluid with a non-uniform velocity profile. Within the boundary layer the reflected shock's velocity relative to the flowing gas is the same as it is outside the boundary layer, but its velocity relative to the fixed coordinate system (the shock tube walls) is higher. An observer with a line-of-sight perpendicular to the wall and parallel to the reflected shock will, therefore, see a density change preceding the visible reflected shock. The width of this part of the reflected shock system will be proportional to the thickness of the boundary layer at each point. Boundary layer thickness, in turn, will be a function of time elapsed after the incident shock's passage and, so, the apparent thickening of the reflected shock will increase as it propagates further upstream. These effects are clearly visible in parts C through G of Fig 15.

Other interesting features visible in this sequence include the formation of a pair of vortices near the junction of the nozzle inlet radii

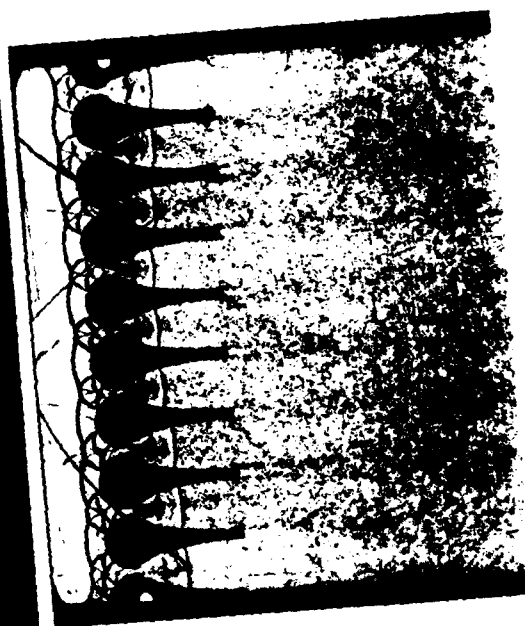
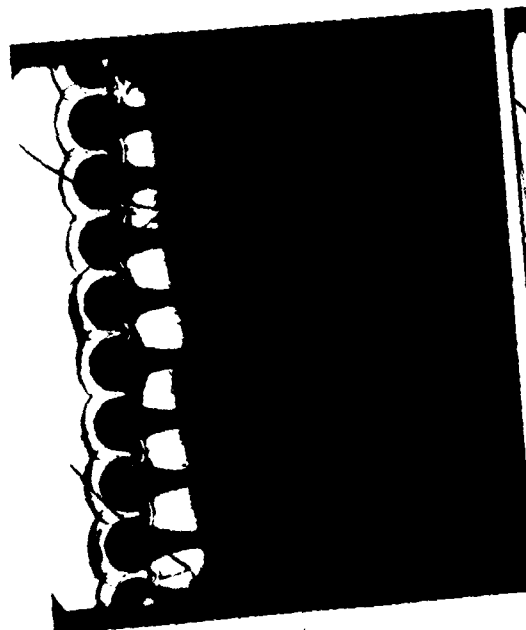
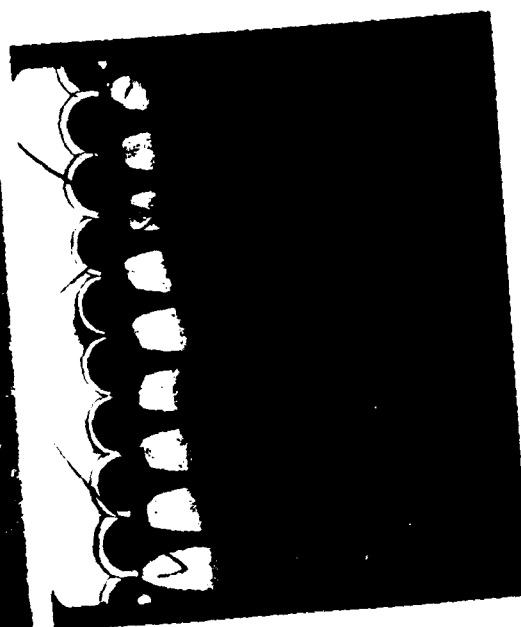
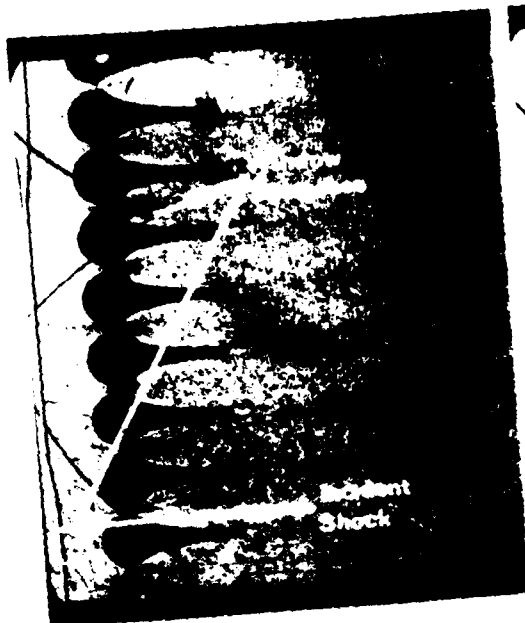
and the nozzle block holders. After formation, the first pair moves laterally and then assumes a relatively stable position in contact with the upstream-facing portion of the nozzle block holders.

The transverse inlet reflected shock pattern development in C and D appears identical to the processes noted in series 4. A straight starting shock has formed in part E as has a single-sided jet on the centerline between starting and incident shocks. G and H clearly show that the entire nozzle has assumed a condition of uniform supersonic flow in that the starting shock has moved downstream out of the nozzle and oblique shocks have formed at the exit plane. The oblique exit plane shocks that are visible in H are characteristic of over-expanded supersonic nozzle operation. A pattern of curved Mach lines is also visible within the nozzle. The entire starting process, from incident shock contact with the inlet to the fully started condition in G occurred in approximately 84 microseconds.

The feature resembling a rotated "W" located downstream of the exit in H has been observed by the author in high-speed motion pictures of rocket engine starting transients.

Series 10

Incident shock strength in this test series was essentially identical with that of series 4, 7, and 8. Figure 17A through P is a sequence of 16 of the 30 closely spaced schlieren photographs taken in this series. Part A of the figure identifies visible components of the multiple-nozzle test section and points out defects in the test section windows. The overall granular appearance of the flow field downstream from the nozzles is due to heavy pitting of the plexiglas that occurred

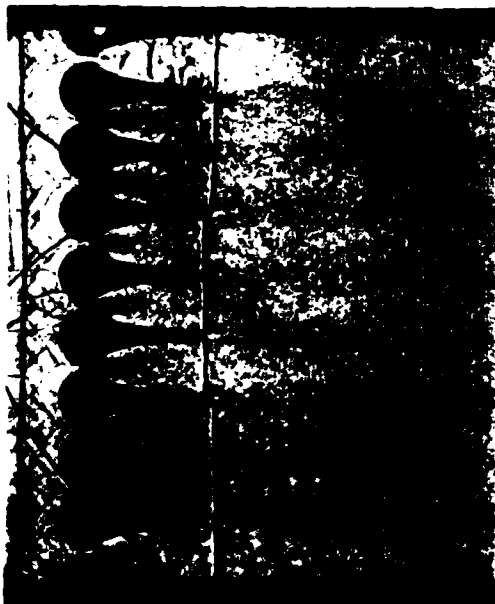




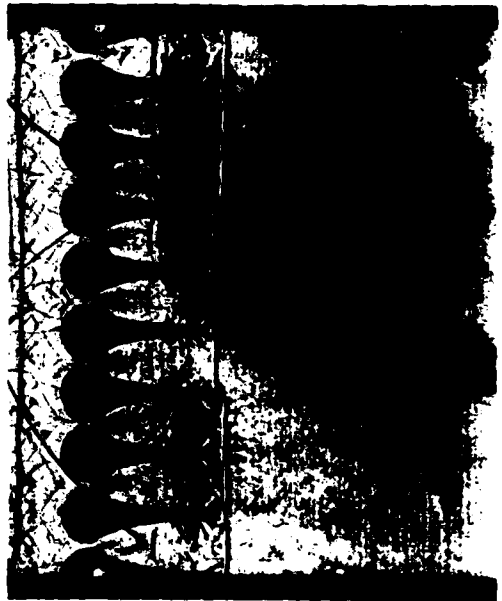
(E) $t = 9.1 \text{ sec}$



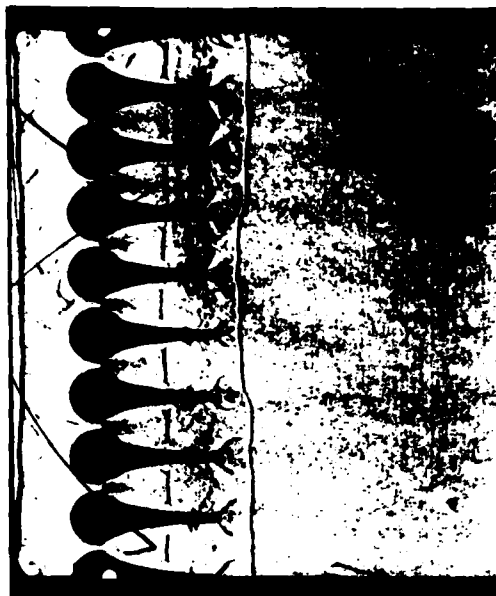
(F) $t = 18.1 \text{ sec}$



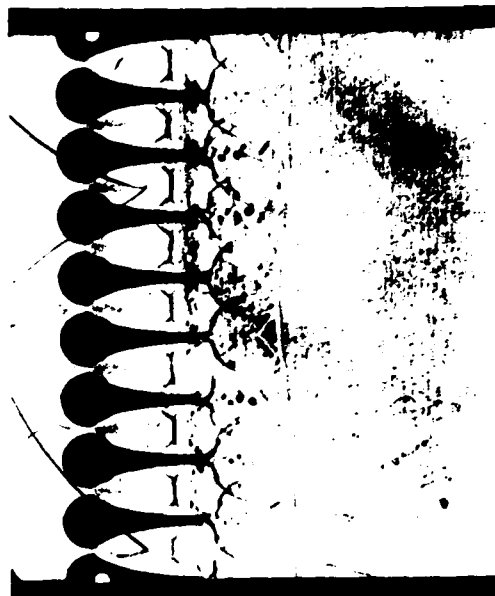
(G) $t = 24.1 \text{ sec}$



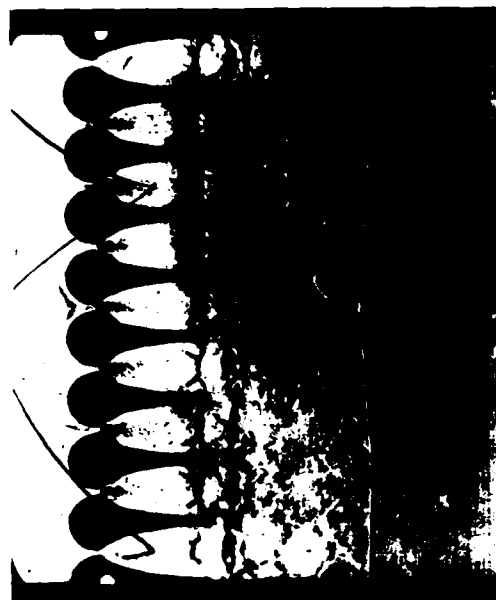
(H) $t = 26.1 \text{ sec}$



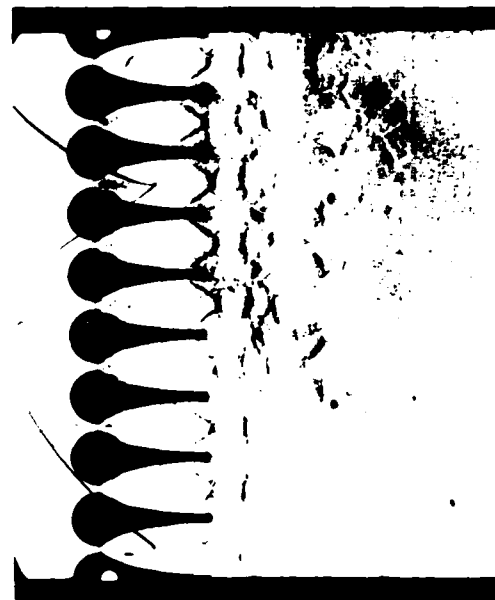
(I) $t = 28.1$ sec



(J) $t = 39.1$ sec

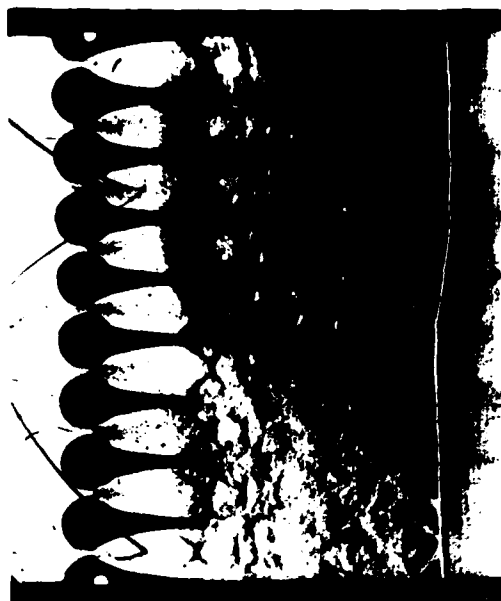


(K) $t = 57.1$ sec

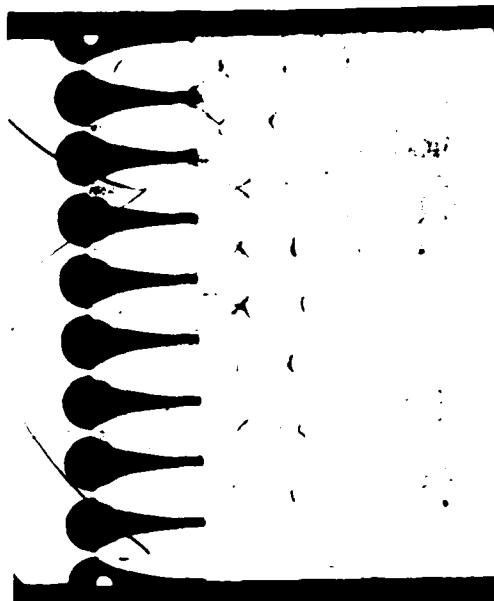


(L) $t = 62.1$ sec

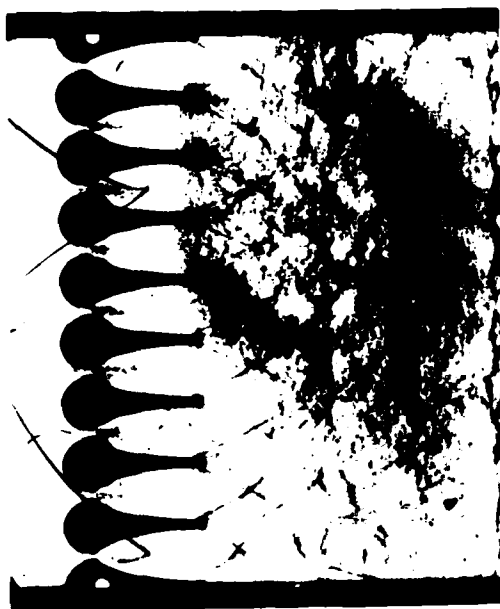
Fig 17. (Continued.)



(M) $t = 75.1 \text{ sec}$



(N) $t = 95.1 \text{ sec}$



(O) $t = 125.1 \text{ sec}$



(P) $t = 130.1 \text{ sec}$

Fig. 17. Continued

during previous use in continuous flow experiments. The pitting is especially heavy at and slightly upstream from the nozzle throats and should not be confused with flow features in this sequence.

Not all of the photographs obtained in series 10 are represented in the shock location versus time of throat passage data plotted in Fig 16 because, as before, the electronic timers used to measure Δt_1 and Δt_2 occasionally failed even though the delay computer and camera functioned properly. Shock location measurements were made only on the centerline of the nozzle formed by blades 5 and 6 (throat number 5 in Fig 5).

The incident shock wave's deviation from a straight normal shock visible in part A of Fig 17 is due to the fact that its interaction with the transverse reflected waves generated at the stabilization chamber-to test section area reduction was not yet completed. This effect was also present in the single nozzle, but was not as visible because of the smaller field of view permitted by the windows in that test section.

The incident shock impinges on the nozzle inlets, undergoes the reflection/penetration process observed in the single nozzle, and produces the characteristic flow features within the nozzle. All this is visible in Fig 17B through G. The incident shock's non-uniform velocity across the nozzle array has clearly persisted in the transmitted incident shocks nearing the nozzle exits in E and F.

Between D and K, each nozzle's starting shock is seen to oscillate from concave toward the throat to concave away from it. This behavior almost certainly occurred in the single nozzle as well, but was not visible because of the greater intervals between photographs.

The incident shock has separated from all nozzles in Fig 17H with the formation of a vortex at the tip of each blade. These vortices result

from slightly different flow expansion rates behind the incident shock around the sharp corners of the blades. This effect did not occur in the single nozzle assemblies, which indicates that the exit "step" failed to accurately simulate adjacent channel flow. The strongest of the vortices are shed from blades 4 and 7 as would be expected from the fact that these blades form the four nozzles across which the almost stepwise discontinuity in the incident shock occurred. Vortices from the other nozzle blade tips are less noticeable from their generation onward and have become indistinguishable from other flow features by the time photograph N was taken. It is interesting to note that the vortices are generated and shed from the same side of the blade ends from one photograph to the next despite the fact that each photograph records a separate event. Which side of a particular blade the first vortex forms on is not a matter of chance: it is determined by the existence of (sometimes small) pressure differences from one throat to the next. Subsequent vortices form in the classical alternating process.

Between I and J of Fig 17, the test section was disassembled for cleaning. The correct throat opening of 0.069 inch was not maintained in the nozzle between blades 9 and 10 upon reassembly. Photographs subsequent to J show that this nozzle's starting shock is expelled slightly later than is the case with the others. It is seen in O that the oblique shocks originating from the downstream tips of the nozzle blades intersect only about 75 percent of the distance downstream attained by corresponding features associated with the other nozzles. This confirms that the throat opening was reduced from the nominal dimension with the effect of raising the design Mach number of this particular portion of the array.

Wagner (Ref 10) observed that an axial misalignment of only 0.003 inch between the throats of a multiple nozzle array operating at a slightly higher Mach number in continuous flow resulted in gross flow distortions from one nozzle to the next. Except in the case of the known error in throat 9 opening size, no similar distortions are evident in this experiment despite the fact that the construction of the test section precluded an alignment accuracy in any axis better than approximately 0.005 inch.

All nozzles in the array are fully started in part N of Fig 17 with the possible exception of the misaligned one. Seventy-nine microseconds have elapsed since the incident shock contacted the inlets of the three center nozzles. This compares well with the 84 microseconds time from the small single nozzle. The former figure is probably more representative because of the closer spacing of the multiple-nozzle test section photographs.

The pressure ratio between the cavity downstream of the nozzle array and the test section entrance resulting from the passage of the incident shock wave was insufficient to attain the uniform supersonic cavity flow essential for gasdynamic laser operation. As noted by Wagner (Ref 10), this is indicated by the presence of ill-defined regions of compression and expansion processes downstream of the exit plane oblique shocks. The pattern persisted in this form (Fig 17P) until all flow dissipated about 200 microseconds after incident shock passage through the throats.

Test series 9D was conducted with the highest shock tube diaphragm pressure ratio attainable (just over 64), but no noticeable change in the nature of the cavity flow was observed. Flow velocity determinations in this series and in series 9A, 9B, and 9C proved impossible because the

test section diffuser blades' bow shock was highly curved and detached. Flow velocity at the diffuser location would not have been representative of conditions within the nozzles anyway because of the dissipative processes occurring in the intervening cavity.

Size Effects

No fundamental differences between the shock induced starting processes in large and small nozzles were observed which can be associated with the boundary layer effects noted by Jindra (Ref 11). In fact, the large single nozzle's failure to start is in opposition to his results which indicated that starting is delayed as size is decreased. Since the two nozzle sizes in this study were known to be proportionally similar to within 0.005 inch and errors at least this large did not prevent starting individual nozzles in the multiple array, it is hypothesized that the large nozzle's failure to start is related to the transverse inlet reflection process.

Specifically, the increase in apparent reservoir pressure (Region 7) following the incident shock is a function of both the strength of this shock and the number of transverse inlet reflections which occur before the incident shock passes out of the nozzle. The frequency of these reflections was lower for any given incident shock strength in the large nozzle simply because of the greater distance between inlet walls. Therefore, the effective reservoir pressure increased more slowly than was the case in the small nozzles and processes underway in the expansion section had time to increase the effective exit plane pressure enough to prevent supersonic flow initiation.

Theoretical Versus Actual Shock Tube Performance

Table II compares test section entrance shock speeds and Mach numbers calculated with the procedure described in Appendix A to those measured during the 13 test series performed. Actual corrected shock tube diaphragm pressure ratio and ambient temperature for each test were used to make the analytical predictions.

All of the predicted shock velocities were higher than those measured except for test series 9D. Here, the measured velocity was 7.5 percent higher than expected. This series was conducted with the maximum available driver pressure of somewhat more than 200 inches of mercury. The uncharacteristically high shock speeds measured may have resulted from the fact that at these pressures the P_4 pressure gage was used outside its calibrated range (above 200 inches mercury), so that the actual driver section pressure may have been substantially higher than the gage indicated.

Despite the above, the differences between predicted and measured shock speeds were almost identical with the systematic measurement errors described in Appendix B--roughly 7 percent. The general trend of the differences probably does indicate a real inaccuracy in the analytical model, however.

Time Delay Computer Performance

Average percent differences between the distance d_2 expected, based on time delay computer adjustments, and the measurements taken from the photographs of the actual distance for test series 1, 4, 7, 8, and 10 are shown in Table III.

The largest of the shock location errors shown in Table III is two orders of magnitude greater than the expected measurement uncertainty

TABLE II
Predicted Versus Actual Test Section
Entrance Shock Speeds

Series	u_{61} ft/sec	M_{61}	$\Delta\%$	\bar{M}_{se}
1	1803.8	1.60	+2.49	1.56
2	2303.1	2.04	+7.10	1.98
3	2712.7	2.40	+7.73	2.33
4	2857.7	2.53	+9.86	2.41
5	2845.7	2.52	+4.37	*
6	2840.7	2.51	+5.56	*
7	2827.7	2.50	+6.89	2.52
8	2840.7	2.51	+7.82	2.53
9A	2829.9	2.51	+6.40	2.34
9B	2838.4	2.51	+7.76	*
9C	2829.6	2.51	+8.37	*
9D	3146.6	2.78	-7.45	*
10	2829.1	2.51	<u>+7.49</u>	2.51
average			+6.82%	

Where:

u_{61} \equiv Predicted Test Section Entrance Shock Speed

M_{61} \equiv Predicted Shock Mach Number at Test Section Entrance
(based on Actual Temperature)

$\Delta\%$ \equiv Percent Error $\left[\frac{u_{61} - \bar{u}}{u_{61}} \right] \times 100$ in Predictions where \bar{u} is from Table I.

\bar{M}_{se} \equiv Average Test Section Entrance Mach Number (based on Δt_2)

* No photographs with incident shock in entrance region

TABLE III
Time Delay Computer Distance Errors

Series	$\Delta d\%$
1	5.6
4	5.3
7	8.0
8	8.7
10	7.9

where:

$$d\% = \frac{d_{2m} - d_{2e}}{d_{2m}} \times 100$$

d_{2m} = Distance from transducer C to incident shock; inches

d_{2e} = Expected distance from transducer C to incident shock; inches

for d_2 calculated in Appendix B. That is: 8.7 percent of the 10.101 inch sensor-to-nozzle throat distance in series 8 equals 0.88 inch, while the expected measurement uncertainty is only 0.0075 inch.

The data plotted in Figs 13 and 16 show that the incident shock's speed remained essentially constant throughout its passage through the nozzle, but the disparity between corresponding entries in the \bar{M}_{s1} column of Table I and the \bar{M}_{se} column of Table II (which are the average incident shock Mach numbers computed with Δt_1 and Δt_2 , respectively) indicate that the shock speed was not constant between the velocity sensors and the camera. This speed change is a violation of the time delay computer's basic operating assumption.

The magnitude of the observed shock velocity change from the region of the sensors to the camera location increases from 0 to about 9 percent

(see Tables I and II) as the incident shock speed increases. The maximum agrees well with the upper limit of shock position errors shown in Table III and is a trend in the direction to be expected if the position errors were due to shock strengthening and acceleration due to an area reduction. The non-zero shock position errors observed in test series 1 despite equivalent shock speeds calculated from Δt_1 and Δt_2 may be explained by considering the sensors used to measure those intervals.

The pressure transducers which sensed shock wave passage and provided input data to the time delay computer have a circular 0.375 inch diameter sensitive surface or diaphragm. As noted in Chapter II, the relationship between transducer voltage output and pressure distribution with time and location across the surface was unknown, but the results of this study indicate certain trends of behavior bearing directly upon the observed shock location errors.

Referring to the oscilloscope traces of amplified transducer outputs shown in Fig C2, it is evident that the incident shock's strength (or velocity) determines both the magnitude of the output signal and its rate of change. The trend here is not in the obvious direction. As the shock strength increases, the magnitude of both decrease. These effects may be ascribed to sensor diaphragm inertia and stiffness qualities, a postulate which is supported by oscillations visible in the output signal immediately after its initial increase. They may be interpreted as resonant vibrations at the diaphragm's natural frequency since that frequency (67 kHz) is basically unchanged over the three photographs in the figure despite the widely different shock speeds (1800 to 2600 feet per second) represented. The oscillations indicate that transducer dynamic response is a significant factor in this application.

The magnitude of the pressure transducer output signal step is irrelevant to the delay computer's operation because it may be compensated for by adjusting the gain of the instrumentation amplifier through which it passes. The slope of the signal step is a different matter because it reflects the relationship between the shock's location on the sensor's diaphragm surface and the time at which the output signal increases to the point at which the delay computer recognizes its presence. If the slope did not change, then it could be assumed that a recognizable output signal was generated when the shock reached the same point on the diaphragm, regardless of its strength. The slope does change: so the actual situation is one in which the effective shock sensor separation distance d_1 is not constant.

Another point to consider is the fact that diaphragm's natural oscillation period of 0.15 microsecond (1/67 kHz) is also the time required for a shock wave traveling at 2100 feet per second to pass over the 0.375 inch diameter diaphragm. Most of the data collected in this investigation involved shock speeds within 500 feet per second of this value. Thus the sensor's performance was rendered more variable by impulsive excitations near their natural periods.

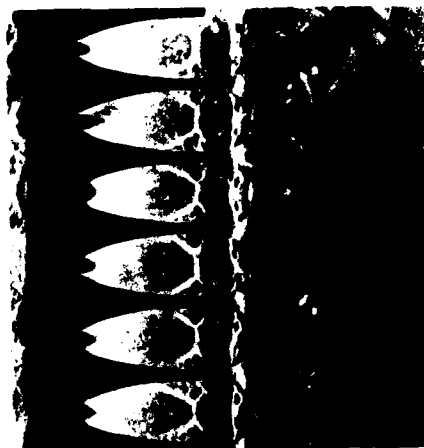
Another factor in the delay computer's overall performance was the spark lamp used for flow field illumination. As the number of discharges after each disassembly and cleaning increased, so did the variation in time between the delay computer's trigger and the lamp's flash.

In their totality, the above observations indicate a complex and undesirable relationship between incident shock strength and shock sensor output signal timing. It is difficult to draw generalized quantitative conclusions concerning the true sources of the incident shock position

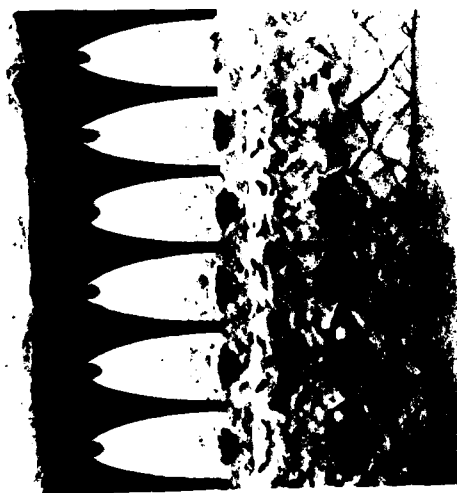
errors in the photographs because of these factors. It is important to note, however, that the time delay computer produced consistent results. Even though the actual photographed shock location might vary as much as 8.7 percent from the preset location, consecutive photographs made with the time delay computer f_2 adjustment unchanged and with approximately the same shock tube diaphragm pressure ratio succeeded in recording the shock in the same location with much less than a 9 percent variation.

Figure 18A and B graphically portray the time delay computer's consistent operation in this study. The photographs are not part of the experimental data and show only throats 3 through 8 of the multiple-nozzle test section. The shock tube diaphragm pressure ratio for both parts of the figure was 32.4 and the resulting incident shock speeds were 2934 and 2927 feet per second, respectively. The measured difference between the incident shock's location in the two photographs was 0.0012 inch. This is less than the expected distance measurement error (from Appendix B) of 0.0075 inch, and therefore, may be considered negligible, as may the difference between the incident shock speeds.

The situation represented by the photographs in Fig 18 may be generalized to one in which pressure transducers of smaller diameter and higher natural frequency than those used in the present study, together with a light source optimized for reliable operation, are employed in a shock tube with no area change between velocity measurement and camera locations. Despite the unknown incident shock speeds in both tests, the time delay computer and associated equipment yield photographs with the disturbance at identical locations on the first two attempts. This performance, or even the 9 percent location errors experienced in this investigation, would be considered either negligible or a significant improvement in many cases.



(A) $u_s = 2934$ feet per second



(B) $u_s = 2927$ feet per second

Fig 18. Time Delay Computer Consistency

IV. Conclusions

The results of this investigation are in general agreement with previous studies involving supersonic nozzles with straight-taper expansion sections. Discordant results may be understood in terms of differences in shock tube operating conditions rather than fundamental differences in the dynamic processes. In this study, Mach 3.2 contoured, rapid expansion, supersonic nozzles with 0.069 inch throat openings and total lengths of 0.904 inches were observed to attain a fully started condition about 80 microseconds after the passage of a Mach 2.33 shock wave. A single nozzle four times this size failed to start for reasons not fully understood at this time.

Intra-nozzle dynamic processes in single and multiple arrays of the nozzle tested were identical. The simulated lasing cavity downstream of the multiple-nozzle array did not achieve a started condition due to the excessive static pressure in the region following the incident shock wave's passage.

No fundamental differences between the large and small nozzle starting processes were observed that could be attributed to boundary layer effects. It is hypothesized that the large nozzle's failure to start under conditions which did start the small nozzles is due to the lower frequency of the transverse inlet reflections in the former.

The digital time delay computer designed for this experiment proved invaluable. It permitted repeatable location of the incident shock in each photograph with no prior knowledge of the shock's propagation

speed. Differences between the preset shock location and the actual photographed location are judged due to the dynamic response characteristics of the pressure transducers used as shock passage sensors.

V. Recommendations

1. Applications of the shock induced starting process to practical gasdynamic laser designs will require further investigation in the following areas:

- A. Achievement of a condition of uniform supersonic flow in the cavity downstream of the multiple nozzle array exit plane.
- B. Shock propagation through channels with right-angle turns typical of existing gasdynamic laser channels.

These investigations would be facilitated by the use of very high speed motion picture equipment to document events throughout the flow field.

2. Further investigation into the details of nozzle inlet shock reflection processes is indicated by the large single nozzle's failure to start under conditions which did produce starting in the small nozzles. Reflection strength and frequency as a function of inlet geometry should be examined over a range of incident shock strengths.

Bibliography

1. Shapiro, Ascher H. The Dynamics and Thermodynamics of Compressible Fluid Flow, Volume I. New York: The Ronald Press Company, 1953.
2. Leipmann, H.W. and A. Roshko. Elements of Gasdynamics. New York: John Wiley & Sons, Inc., 1957.
3. Smith, C. Edward. "The Starting Process in a Hypersonic Nozzle," Journal of Fluid Mechanics, 24(4):625-640 (1966).
4. Amann, H.O. "Experimental Study of the Starting Process in a Reflection Nozzle," Shock Tube Symposium, The Physics of Fluids Supplement I (1969), pp I-150-I-153.
5. Gvozdeva, L.G and Yu. V. Zhilin. "Experimental Investigation of Gasdynamic Processes at Sudden Start-up" (Translation), Zhurnal Prikladnoi Mekhaniki i Tekhnicheskoi Fiziki, No 4, pp. 66-74 (July-August 1977). UDC 533.6.011:533.697.
6. Leverage, Robert A., Elihu Zimet and Eva M. Winkler. "Interferometric Studies of the Flow in Fast-Expanding Nozzles," NOLTR-73-61, Naval Ordnance Laboratory, White Oak, Silver Spring, Maryland, 19 March 1973.
7. Egan, Douglas S, Jr., 1Lt, USAF, and Robert A. Foster, 1Lt, USAF. "Gas Dynamics Research with the Air Force Institute of Technology Shock Tube." Master's Thesis. Air Force Institute of Technology, Wright-Patterson AFB, OH, August 1956.
8. Holder, D.W. and R.J. North. Optical Methods for Examining the Flow in High-Speed Wind Tunnels, Part I: Schlieren Methods. AGARDOGRAPH 23. North Atlantic Treaty Organization, Advisory Group for Aeronautical Research and Development, Paris, France, November 1956.
9. Zhilin, Yu. V., T.V. Bazhenova and L.G. Gvozdeva. "Bifurcation of the Shock Wave Upon Reflecting From the End Wall of the Shock Tube," Archiwum Mechaniki Stosowanej, 30:675-681 (1978).
10. Wagner, Jerry L. "A Cold Flow Field Experimental Study Associated with a Two-Dimensional Multiple Nozzle," NOLTR 71-78. Naval Ordnance Laboratory, White Oak, Silver Spring, Maryland, 1 July 1971. AD 731677.
11. Jindra, Karl J., 2Lt, USAF. "Geometric Effects on the Performance Characteristics of Very Small Nozzles," Master's Thesis. Air Force Institute of Technology, Wright-Patterson AFB, OH, 1971.

12. Glass, I.I. and J. Gordon Hall. Handbook of Supersonic Aerodynamics, Section 18, "Shock Tubes." NAVORD Report 1488, Volume 6. Washington: Government Printing Office, December 1959.
13. Ames Research Staff, Ames Aeronautical Laboratory, Moffett Field, CA. Equations, Tables, and Charts for Compressible Flow. NACA Report 1135, 1953.
14. Whitham, G.B. "On the Propagation of Shock Waves Through Regions of Non-Uniform Area or Flow," Journal of Fluid Mechanics, 4:337 (1958).
15. Tamba, Mohammed Latif, SqLdr, PAF. "The Interaction of a Moving Shock With an Abrupt Area Reduction in a Shock Tube." Master's Thesis. Air Force Institute of Technology, Wright-Patterson AFB, OH. 1970.
16. Holman, J.P. Experimental Methods for Engineers. New York: McGraw-Hill Book Company, 1971.

APPENDIX A

Nozzle Design Selection

Gasdynamic laser flow channel nozzles normally operate at design Mach numbers of 3 or higher. This was considered the minimum Mach number of a nozzle suitable for this study. According to Hall and Glass (Ref 12: 413), a constant area air-air shock tube is capable of generating a $M = 6.19$ shock wave; but this requires an infinite diaphragm pressure ratio. The maximum shock speed attainable in the 4 by 8 inch section of the AFIT shock tube was approximately $M = 1.89$. A reduced area section was, therefore, employed as a shock strengthening device ahead of the test section. Hardware suitable for this purpose consisted of a straight-taper converging section and a 48 inch long stabilization chamber with a 1 inch by 4.5 inch cross-section.

Given the available shock tube configuration, a calculation procedure was developed to predict the strength of the shock arriving at the test section in terms of its speed and pressure ratio. This procedure was based on the following assumptions:

- 1) Perfect gas behavior of air with constant $\gamma = 1.4$
- 2) Normal shock behavior according to the adiabatic and/or perfect gas relations of NACA TN 1135 (Ref 13)
- 3) Normal shock strengthening at reduced area duct sections according to Whitham's results (Ref 14), also known as Whitham's Rule.

Figure 10 defines the regions used in these calculations.

The first step in the procedure was solution of the shock tube equation given by Leipmann and Róshko (Ref 2:81) for a given diaphragm pressure ratio P_{41} . The resulting normal shock pressure P_{21} was converted into an incident shock Mach number M_1 , and Whitham's Rule (after Tamba, Ref 15) applied to obtain the Mach number of the shock transmitted into the reduced area section. Again after Tamba, it was assumed that the transmitted shock had reached "steady-state" conditions by the end of the stabilization chamber so a normal shock reflection was calculated from the test section.

As a gross simplification of the highly dynamic conditions existing within the nozzle during the incident shock's passage, it was assumed that the static pressure behind the normal shock reflection from the test section, P_7 , was in effect a nozzle reservoir pressure and that the shock tube driven end pressure P_1 was an exit plane static pressure. The standard isentropic, perfect gas relation between static and total pressure as a function of Mach number for steady supersonic flow was then used to calculate the flow Mach number necessary to produce a ratio equal to $P_7/P_1 = P_{71}$. In the simplified model, this pressure ratio was assumed to be that existing across the nozzle. The result was a prediction of the design Mach number of a nozzle optimized for the pressure ratio induced at the test section by the given shock tube diaphragm pressure ratio.

A FORTRAN computer code was written to implement the procedure and used to calculate nozzle design Mach numbers at intervals over the shock tube's operating range of $0 < P_{41} < 100$. These calculations indicated that with the maximum available driver pressure of just over 200 inches of mercury and the minimum driven end pressure expected to be possible of approximately 2.0 inches of mercury, a Mach 3.19 nozzle was appropriate.

Based upon this, and the fact that transverse nozzle inlet reflections were expected to raise the "apparent reservoir" pressure P_7 above the post-reflection static pressure, an existing rapid expansion nozzle design optimized for Mach 3.2 continuous flow operation was selected for the experiment.

The computer code was also employed to calculate expected shock parameters at the corrected diaphragm pressure ratios actually used during testing.

APPENDIX B

Experimental Errors and Data Reduction

The accuracy of the quantitative information presented in this report is subject to certain systematic errors that were inherent in the measurements upon which the information is based. The magnitude of the effect of these errors on various quantities reduced from the measurements is discussed below along with a description of how the data reductions were performed.

The method described by Holman (Ref 16:37) is used to calculate estimates of the experimental uncertainties in the reduced data. In this method, if Z is the calculated quantity for which an error estimate is desired, then:

$$w_Z = [(\frac{\partial Z}{\partial x_1} w_1)^2 + (\frac{\partial Z}{\partial x_2} w_2)^2 + \dots + (\frac{\partial Z}{\partial x_n} w_n)^2]^{1/2} \quad (B-1)$$

where:

$w_Z \equiv$ Error estimate in the dependent quantity Z

$w_n \equiv$ Measurement uncertainty in the independent quantities x_n

$x_n \equiv$ Set of measurements upon which Z depends

This equation is evaluated for each member of the set of data for which the dependent quantity Z is calculated, or it may be evaluated at appropriate points within the set to determine error bounds.

1. Shock Speed

$$u = \frac{d}{t} \quad (B-2)$$

$$w_u = [(\frac{\partial u}{\partial d} w_d)^2 + (\frac{\partial u}{\partial t} w_t)^2]^{1/2} \quad (B-3)$$

where:

$u \equiv$ Shock wave propagation velocity, feet per second

$d \equiv$ Measured distance between shock wave locations at time t ;
inches

$t \equiv$ Measured elapsed time between known shock locations; seconds

$w_u \equiv$ Uncertainty in shock velocity; feet per second

$w_d \equiv$ Uncertainty in shock location; inches

$w_t \equiv$ Uncertainty in elapsed time; seconds

Two distance measurements were used to calculate shock speeds: separation d_1 between shock sensors B and C (Fig 7), and distance d_2 from sensor C to the shock's location in the photograph. Shock sensor separation was 2.0 ± 0.01 inches between geometric centers of the sensors. No data was available on the relationship between sensor geometric centers and the points on their diameters at which the maximum electrical output would occur as the shock passed. These points were, therefore, assumed to coincide. Location of the incident and starting shocks in each photograph was determined with a moving-stage-equipped 60 power microscope having a cross-hair reticle and a micrometer scale and corrected for photograph scale by measuring visible features of known size. Each measurement was performed three times and the results averaged. When combined with the distance measurement from shock sensor C to the nozzle throat in each test section, the measurement accuracy was ± 0.05 inch.

Time measurements consisted of the post-test readings on two Hewlett-Packard model 5325B digital counter/timers. Both were within their calibration periods and operated with an established accuracy of ± 0.1 microsecond in the manner employed. Sensitivity adjustments of the timers' start and stop circuits were extremely critical so that the occasional timer failures observed consisted of failures to start or stop. Times indicated after shock tube shots in which the timers started and stopped properly were assumed accurate to the above specification. Time Δt_1 was the interval between signals representing shock wave traverse of distance d_1 ; time Δt_2 was the interval between the shock's arrival at sensor C and the time at which the photograph was taken.

After taking appropriate partial derivatives and inserting uncertainty values, the error estimate becomes:

$$\text{for } d_1: \quad w_u = \left[\left(\frac{0.01}{t} \right)^2 + \left(\frac{-0.1 \times 10^{-6} d}{t^2} \right)^2 \right]^{1/2} \quad (\text{B-4})$$

$$\text{for } d_2: \quad w_u = \left[\left(\frac{0.05}{t} \right)^2 + \left(\frac{-0.1 \times 10^{-6} d}{t^2} \right)^2 \right]^{1/2} \quad (\text{B-5})$$

Taking tests from series 1 and 7 as representative, and substituting into these expressions times and distances measured when the incident shock wave is nearest the nozzle throat, the shock speed errors are calculated:

$$\text{Series 1: for } d_1, \quad w_u = \left[\left(\frac{0.01}{99.6 \times 10^{-6}} \right)^2 + \left(\frac{-0.1 \times 10^{-6} \times 2.0}{(99.6 \times 10^{-6})^2} \right)^2 \right]^{1/2} = 102.4 \text{ fps} \quad (\text{B-6})$$

$$\text{for } d_2, \quad w_u = \left[\left(\frac{0.05}{386 \times 10^{-6}} \right)^2 + \left(\frac{-0.1 \times 10^{-6} \times 8.113}{(386 \times 10^{-6})^2} \right)^2 \right]^{1/2} = 129.6 \text{ fps} \quad (\text{B-7})$$

$$\text{Series 7: for } d_1, \quad w_u = \left[\left(\frac{0.01}{62.7 \times 10^{-6}} \right)^2 + \left(\frac{-0.1 \times 10^{-6} \times 2.0}{(62.7 \times 10^{-6})^2} \right)^2 \right]^{1/2} = 167.4 \text{ fps} \quad (\text{B-8})$$

$$\text{for } d_2, w_u = \left[\left(\frac{0.05}{294 \times 10^{-6}} \right)^2 + \left(\frac{-0.1 \times 10^{-6} \times 10.21}{(294 \times 10^{-6})^2} \right)^2 \right]^{1/2} = 170.5 \text{ fps} \quad (\text{B-5})$$

As percentages of the measured speeds:

$$\text{from (B-4):} \quad \frac{w_u}{u} \times 100 = \frac{102.4}{1673.7} = 7.2\% \quad (\text{Series 1; } d_1)$$

$$\text{from (B-5):} \quad \frac{w_u}{u} \times 100 = \frac{129.6}{1769.8} = 7.3\% \quad (\text{Series 1; } d_2)$$

$$\text{from (B-4):} \quad \frac{w_u}{u} \times 100 = \frac{167.4}{2658.2} = 6.3\% \quad (\text{Series 7; } d_1)$$

$$\text{from (B-4):} \quad \frac{w_u}{u} \times 100 = \frac{170.5}{2895.1} = 5.9\% \quad (\text{Series 7; } d_2)$$

Distance measurement errors dominate these figures.

2. Mach Number

Assuming perfect gas behavior with constant $\gamma = 1.4$,

$$R = 53.3498 \frac{\text{ft-lbf}}{\text{lbm-}^\circ\text{R}}, \text{ and } g_c = 32.174 \frac{\text{lbm-ft}}{\text{lbf-sec}^2} :$$

$$M = \frac{u}{a} = \frac{u}{49.02\sqrt{T}} \quad (\text{B-6})$$

$$w_M = \left[\left(\frac{w_u}{49.02\sqrt{T}} \right)^2 + \left(\frac{-w_T u}{49.02(T)^{3/2}} \right)^2 \right]^{1/2} \quad (\text{B-7})$$

where:

$M \equiv$ Shock propagation Mach number

$u \equiv$ Speed of sound in the gas through which the shock is passing;
feet per second

$T \equiv$ Absolute temperature of the gas; degrees Rankine

$w_u \equiv$ Uncertainty in the velocity measurement; feet per second

$w_T \equiv$ Uncertainty in the ambient temperature measurement; degrees
Rankine

$w_M \equiv$ Measured Mach number uncertainty

Ambient temperature was measured with an accuracy of ± 0.1 degree. Using this, a typical ambient temperature of 529.7 degrees, and the largest of the expected velocity measurement uncertainties from above, the expected Mach number uncertainty becomes:

$$w_M = \left[\left(\frac{102.4}{49.02 \sqrt{529.7}} \right)^2 + \left(\frac{-0.1 \times 1637.7}{49.02 (529.7)^{3/2}} \right)^2 \right]^{1/2} = 0.0908 \quad (B-7)$$

or 6.1 percent of the calculated Mach number.

3. Pressure and Pressure Ratio

True shock tube driver end pressure was calculated from:

$$P_4 = P_i C + P_A \quad (B-8)$$

where:

$P_4 \equiv$ Corrected driver section absolute pressure; inches of mercury

$P_i \equiv$ Bourdon-type gage indicated pressure; inches of mercury

$C \equiv$ Gage error correction factor; $C = 1.003$

$P_A \equiv$ Corrected ambient pressure; inches of mercury

Uncertainties in these measurements were:

$w_{P_i} \equiv 0.05$ inches of mercury

$w_C \equiv 0.0005$ inches of mercury

$w_{P_A} \equiv 0.01$ inches of mercury

For an indicated pressure of 200 inches of mercury and an ambient pressure of 29.92 inches of mercury, the expected P_4 uncertainty is 0.112 inches of mercury or 0.0552 psi.

True shock tube driven end pressure was calculated from the indicated heights in the U-tube manometer from:

$$P_1 = P_A - (h_l + h_r) \quad (B-9)$$

where:

$P_1 \equiv$ Corrected driven end absolute pressure; inches of mercury

$P_A \equiv$ Corrected ambient pressure; inches of mercury

$h_l \equiv$ Height of left mercury column; inches

$h_r \equiv$ Height of right mercury column; inches

Measurement uncertainties were ± 0.05 inch in column height and ± 0.01 inch of mercury in ambient pressure. The error equation becomes:

$$\begin{aligned} w_{P_1} &= [(0.01)^2 + (0.05)^2 + (0.05)^2]^{1/2} = 0.0714 \text{ inches of mercury} \\ &= 0.0351 \text{ psi} \end{aligned} \quad (B-10)$$

Applying the error equation to $P_{41} = \frac{P_4}{P_1}$ yields:

$$w_{P_{41}} = \left[\left(\frac{w_{P_4}}{P_1} \right)^2 + \left(-\frac{P_4 w_{P_1}}{P_1^2} \right)^2 \right]^{1/2} \quad (B-11)$$

where:

$w_{P_{41}} \equiv$ Uncertainty in the diaphragm pressure ratio; inches of mercury

$w_{P_4} \equiv$ Uncertainty in the P_4 pressure measurement; inches of mercury

$w_{P_1} \equiv$ Uncertainty in the P_1 pressure measurement; inches of mercury

$P_1 \equiv$ Corrected driven section pressure measurement; inches of mercury

$P_4 \equiv$ Driver section pressure measurement; inches of mercury

Using uncertainty values for the pressures calculated above and average absolute pressure readings typical of test series 4, 7, 8, and 10 in this relation yields

$$w_{P_{41}} = \left[\left(\frac{0.0714}{6.40} \right)^2 + \left(\frac{0.112 \times 230.9}{(640)^2} \right)^2 \right]^{1/2} = 0.631 \text{ inches of mercury} \quad (B-11)$$

or 0.310 psi, which is 1.75 percent of the indicated pressure ratio.

4. Time Delay Computer

The distance between the second velocity sensor and the point at which the photograph is to be taken, assuming a constant shock speed between sensors and camera, and the expected uncertainty in this distance are given by (see Fig 7):

$$d_2 = \frac{f_1}{f_2} d_1 \quad (B-12)$$

$$w_{d_2} = \left[\left(\frac{\partial d_2}{\partial f_2} w_{f_2} \right)^2 + \left(\frac{\partial d_2}{\partial f_1} w_{f_1} \right)^2 + \left(\frac{\partial d_2}{\partial d_1} w_{d_1} \right)^2 \right]^{1/2} \quad (B-13)$$

where:

$d_2 \equiv$ Distance of the shock from the second speed sensor to the point at which the shock is to be located when the photograph is taken; inches

$f_1 \equiv$ (Constant) frequency of the delay computer up clock; Hz

$f_2 \equiv$ Frequency of the delay computer down clock; Hz

$d_1 \equiv$ Separation between shock velocity sensors; inches

$w_{d_2} \equiv$ Uncertainty expected in the shock's location in the photograph; inches

$w_{f_2} \equiv$ Uncertainty in down clock frequency; Hz

$w_{f_1} \equiv$ Uncertainty in up clock frequency; Hz

$w_{d_1} \equiv$ Uncertainty in shock sensor separation distance; inches

Two Computer Measurements Corporation type 726C digital counter/timers were used to monitor clock frequencies f_1 and f_2 . Their accuracy in the mode in which they were operated was ± 0.1 mHz. As discussed earlier, distance d_1 was known to an accuracy of ± 0.05 inch. With $d_1 = 2.0$ inches,

$f_1 = 10.000$ mHz, and $f_2 = 2.5$ mHz (which gives $d_2 = 8.0$ inches according to Eq 1 in Chapter II), the error equation yields an uncertainty of 0.0075 inch independent of the distance d_2 involved.

The theoretical maximum shock location accuracy possible with the time delay computer is directly proportional to the shock speed and inversely proportional to the up-clock operating frequency f_1 . This accuracy may be represented by the ratio of shock speed to clock frequency as the distance the shock can travel between clock pulses if its velocity remains unchanged between the first velocity sensor and the camera location. For example, if the shock speed is 3000 feet per second and f_1 is 10.000 mHz, the shock can travel 0.0036 inch between pulses. This is the maximum possible accuracy with which the shock's location in the photograph may be pre-determined. Since 3000 feet per second is near the upper limit of shock speeds attained in this investigation, the primary source of expected shock location error is the measurement uncertainty presented in the previous paragraph.

If the shock wave's propagation velocity is not constant over the distance from the region in which the delay computer makes its measurement to the camera location, then the actual distance d_2 become a simple linear function of the ratio of the average velocity between sensors and the average velocity between sensors and camera:

$$d_{2 \text{ non-constant velocity}} = \frac{u_2}{u_1} d_{2 \text{ constant velocity}}$$

The complete sequence of still photographs obtained in test series 1, 4, 7, 8, and 10 was photographed with a motion picture camera, one frame at a time. When projected at normal continuous frame rates, these

motion pictures form a good simulation of the real motion of the flow field that occurred during the events represented by each still photograph. The film was viewed repeatedly as an aid in describing the dynamic flow processes investigated.

APPENDIX C

Time Delay Computer Design and Operation

Figure C1 is a schematic diagram of the brassboard version of the time delay computer used in this study. It functions in the following fashion.

Transistors Q1 and Q2 serve as input buffers and inverters to convert the positive-going instrumentation amplifier output pulses to negative-going transitions required by IC1 and IC2. They are operated as unbiased saturated switches in which the minimum "on" input voltage is set by base-circuit voltage dividing resistors R1 and R2.

Integrated Circuits IC1 and IC2 are one-shot multivibrators wired to produce a single 30 nanosecond output pulse each time their inputs go low. As shown by the oscilloscope traces in Fig C2, the amplified shock sensing pressure transducer signals rise very rapidly (over 100×10^6 volts/sec) and stay high throughout the period of time delay computer operation. Thus, IC1 and IC2 are fired only once during each shock passage.

IC1's output pulse is generated when the incident shock passes sensor B, signifying the beginning of the shock speed measurement. The pulse is coupled to the preset input of IC3A, one-half of a dual flip-flop. IC3A's Q1 output is anded with the up-clock oscillator in IC4A, one-fourth of a quad nand gate and, upon transition, applies the oscillator signal to the count-up input of the 6 decade BCD up-down counter chain formed by IC5 through IC10.

When the shock wave's passage causes an output from sensor C, IC2's one-shot pulse presets IC3B, the $\bar{Q}2$ output of which clears IC3A,

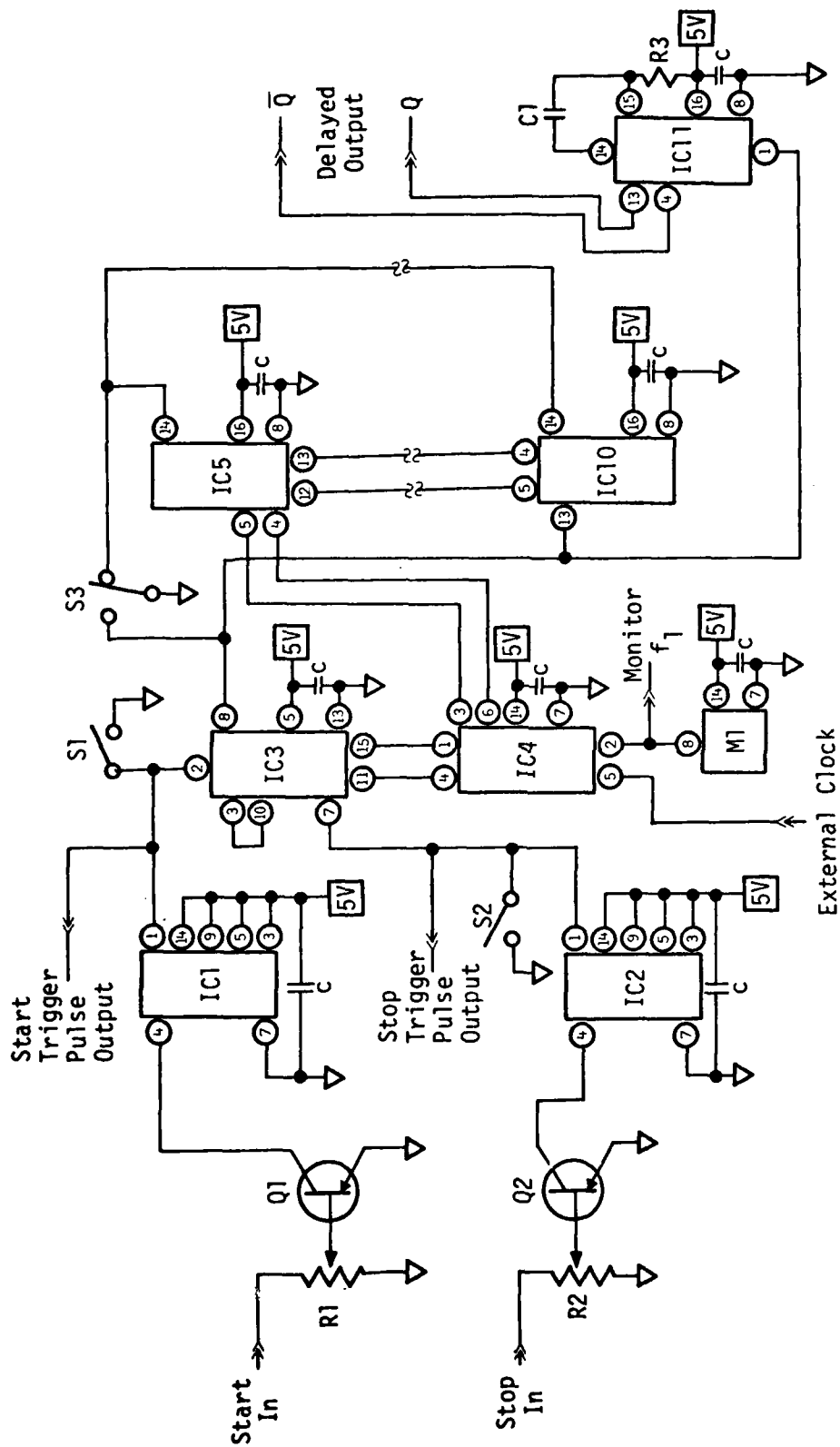


Fig C1. Time Delay Computer Schematic

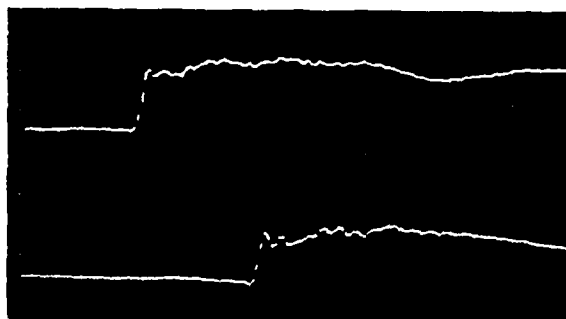


Fig. 11. Detector and Sample Traces

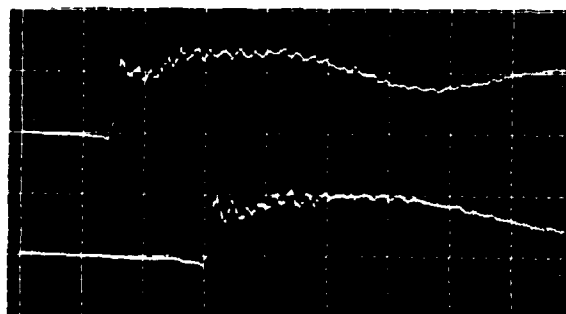


Fig. 12. Detector and Sample Traces

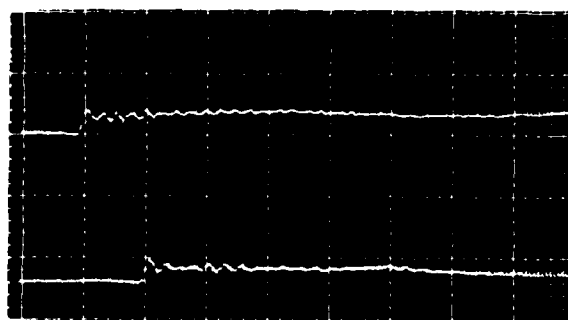


Fig. 13. Sample Abs. 5 V Div Vertical

Fig. 12. Sample Oscilloscope Traces
(All 50 sec Div Horizontal)

Time Delay Computer Parts List

Q1, Q2	2N2222A	Silicon Transistor
IC1, IC2	SN74121	Monostable Multivibrator
IC3	SN7476	Dual J-K Flip-Flop
IC4	SN7400	Quad Nand Gate
IC5-IC10	SN74192	BCD Up-Down Counter
IC11	SN74123	Dual Monostable Multivibrator
R1, R2	10 k Ω	Miniature Trimmer
R3	1 k Ω , 10%	Composition
C	0.1 μ F, 60 v	Ceramic Capacitor
C1	1.0 μ F, 60 v	Ceramic Capacitor
M1	k1091A	10.000 mHz Crystall Oscillator Module (Motorola)

thus disconnecting the up-clock oscillator from the counter chain. IC3B's Q2 output is anded with the variable down-clock oscillator in IC4B, so that this clock is applied to the counter chain count-down input within one clock pulse of the up-clock's disconnection.

The borrow-out output of the counter chain's most-significant-digit counter, IC10, is connected both to IC3B's clear input and to the clock input of IC11, a one-shot multivibrator wired for a single 50 micro-second output pulse. When the counter chain reaches zero after counting down from the up-clock total at a rate determined by the down clock frequency, IC10's borrow-out pulse simultaneously disconnects the down-clock from the chain and produces the system's delayed output pulse through IC11.

The delay computer's up-clock oscillator (f_1) is an on-board crystal controlled module (M1) operating at 10.000 ± 0.0001 MHz. The down clock signal (f_2) comes from an external function generator configured for TTL 50% duty cycle square wave output with a frequency range of 0 to 5 MHz. The external oscillator, a Wavetek model 186, has been found to change frequency in a random fashion by about 3 to 5 kHz during the time when it is electrically connected to the counter chain. It is, therefore, necessary to functionally check the down clock frequency by "dry-cycling" the system and measuring the time required for the counter chain to count completely around (10^6 counts). This is accomplished by triggering the delay computer stop input with no start input. Switches S1 and S2 permit manual triggering and switch S3 clears the counter chain and all flip-flops. It also generates an immediate output pulse.

IC1 and IC2 pulse outputs are made externally accessible as start and stop channel pulse outputs. These signals may be used to trigger external digital timers.

The device was constructed on a phenolic etched printed circuit board and mounted in an aluminum box. A parts list follows the schematic.

Circuit board temperatures were found to rise enough to seriously affect integrated circuit operation without forced convective cooling, so a small, 110-volt fan was mounted on the top of the box.

A patent application has been filed on the design described above. Domestic production and use rights are to be assigned by the author to the United States Government.

APPENDIX D

Silicon Controlled Rectifier Spark Lamp Trigger

The purpose of this circuit is to produce a positive output voltage pulse of approximately 200 volts amplitude when triggered by a positive voltage pulse in the range of 2 to 10 volts. Components are identified in the schematic below.

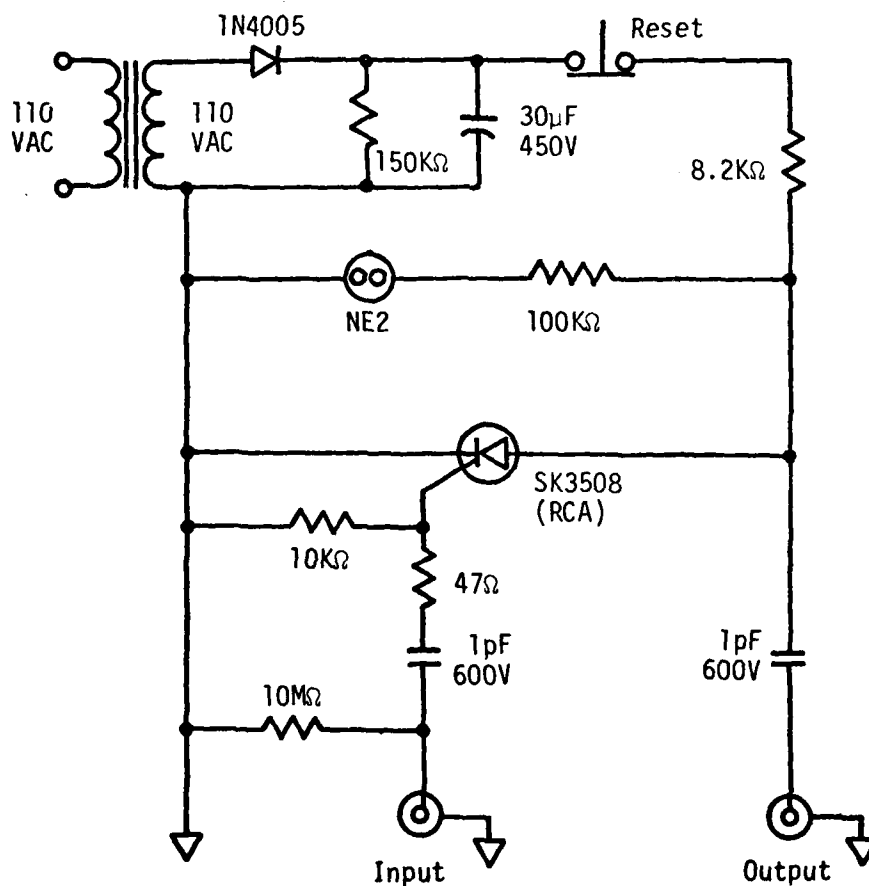


Fig D-1. Trigger Schematic

APPENDIX E

Equipment Control Adjustments

Oscilloscope Tektronix Model 549

Horizontal Display - Channel A

Time/cm: 50 μ sec (calibrated)

Sweep: Single sweep

Triggering

Mode: Trigger

Slope: +

Coupling: AC

Source: External

Level: Approximately 1 o'clock

Stability: Preset

Display: Full Screen Storage

Type M Plug-in Unit

Display: Chopped

Volts/cm: 5 or 10

Mode: Normal: AC

Gain: Calibrated

Position: As required

Computer Measurements Corporation 726C Digital Universal Counter/Timers (Delay Computer)

Function: Frequency A

Scale: 10^4 (red)

Display: Variable

Gate: Auto

Trigger Level Channel A: 6.4 volts

Trigger Slope: (-)

Hewlett-Packard 5325B Digital Universal Counter Timers $\Delta t_1, \Delta t_2$

Sample Rate: Off/Hold

Time Base: 0.1 μ sec

Mode: T.I. A to B (Time Interval A to B)

Channel A and B Input Signals

Attenuation: x10

Mode: AC

Slope: (-)

Level: Approximately 11 o'clock

Inputs: SEP (separate)

Wavetek Model 186 Function Generator

Frequency Range: x1m

Symmetry: Normal

General Mode: Cont

Waveform: (Positive Pulse) ; Norm

Attenuation: 0

Output: Pulse Out (TTL)

AD-A079 879 AIR FORCE INST OF TECH WRIGHT-PATTERSON AFB OH SCH00--ETC F/G 20/5
SHOCK INDUCED STARTING OF GASDYNAMIC LASER NOZZLES.(U)
DEC 77 P A WEBER
UNCLASSIFIED AFIT/GAE/AA/79D-18 NL

2 of 2

AD-A079 879



END
DATE
FILMED
2-80
BDC

APPENDIX F

Schlieren Camera Alignment Procedure

1. Set parabolic mirrors, camera, knife-edge, and plane mirror heights to match height of the test section. The centers of the parabolic mirrors must coincide with a line exactly perpendicular to the shock tube axis (Refer to Fig 9 for general arrangement).
2. Mount a ground glass screen with cross-hairs and features of known size on the camera film plane. Illuminate the ground glass with a high-intensity lamp directed along the axis of the optical path with the camera shutter open. Move knife edge clear of the light cone.
3. Adjust plane mirror on camera rail so that the light cone falls on the center of the parabolic mirror on the camera side of the test section. Adjust the parabolic mirror so that an in-focus image of the ground glass reticle falls on the test section window and is centered in the desired location. The size of the reticle image projected on the test section is inversely proportional to the size of the test section image which will be photographed. That is, if the reticle image is larger than full size, then the photographed image of the test section will be smaller than full size and vice-versa. Coarse adjustments in the reticle image size are made by changing the distance between the parabolic mirror and the test section. Fine adjustments, which also determine the point at which the reticle image focuses, are made by sliding the camera ground glass holder back and forth along the rail.
4. Adjust the light source side parabolic mirror so that the light cone

passing through the test section strikes its center. If both parabolic mirrors are truly perpendicular to the shock tube axis, no adjustment will be necessary.

5. Move the spark lamp so that the front electrode gap is exactly one focal length (30 inches in this case) from the parabolic mirror and then adjust the mirror so that the light cone reflected from it is centered on the electrode.

6. Move the knife-edge into the light cone and adjust it along the camera rail so that its edge is in focus on the spark lamp electrode. Adjust the knife-edge laterally so that the edge exactly bisects the electrode gap.

The knife-edge is now set at the center-focus point of the optical system. Moving the knife-edge aft (toward the film plane) causes the schlieren system to be optimized for vertical flow features; movements forward yield maximum sensitivity to horizontal flow features. Final knife-edge adjustments should be made with trial photographs.

APPENDIX G

Experimental Procedure

Two test parameters could be selected before each shock tube test: approximate shock strength by means of the diaphragm pressure ratio and shock location at the time of the photograph by means of the time delay computer. Because of the time delay computer, each shock's location in the test section could be selected independently of the exact shock speed obtained. The sequence of events leading to each flow field photograph was as follows:

1. Zero all digital timers and the oscilloscope.
2. Adjust delay computer for desired shock location.
3. Clean shock tube and install appropriate thickness of diaphragm material.
4. Close P_4 and P_1 bleed valves; open P_4 and P_1 gage shutoff valves.
5. Start vacuum pump; open P_4 pressurization valve. Set desired diaphragm pressure ratio by bleeding to compensate for system leakage.
6. Extinguish room lights; remove film pack darkslide; cock camera shutter.
7. Open camera shutter (closes automatically after 1/2 second).
8. Remotely rupture diaphragm within 1/2 second of tripping shutter.
9. Close P_4 pressurization valve; shut off vacuum pump; open P_4 bleed valve; open gage shutoff valves.
10. Replace film holder darkslide; remove and develop film.

11. Read and record digital timers.

12. Mark photograph to correspond with recorded data.

Oscilloscope traces were photographed occasionally for use as a diagnostic tool to verify proper signal levels and waveforms and to provide a rough verification of proper digital timer performance. Figure C-2 contains examples of the traces obtained during tests.

Vita

Paul Allen Weber was born on September 19, 1945 at Kelly Field, San Antonio, Texas. After graduating from Elgin High School, Elgin, Oklahoma, he served four years in the U.S. Air Force and then attended and graduated from the University of Oklahoma with a B.S. in Aerospace Engineering in 1973. After receiving an Air Force R.O.T.C. commission, he was assigned to the Air Force Armament Laboratory at Eglin Air Force Base, Florida from February 1974 until his reassignment to the Air Force Institute of Technology in May 1978.

Captain Weber is married to the former Suzanne LaParche of Duncan, Oklahoma. They have two sons, David and Mark. His permanent mailing address is at his parents' residence in care of LtCol (USAF, Ret) and Mrs. Arthur R. Weber, Rt. 1, Box 63, Elgin, Oklahoma, 73538.

UNCLASSIFIED

SECURITY CLASSIFICATION OF THIS PAGE (When Data Entered)

REPORT DOCUMENTATION PAGE		READ INSTRUCTIONS BEFORE COMPLETING FORM
1. REPORT NUMBER AFIT/GAE/AA/79D-18	2. GOVT ACCESSION NO.	3. RECIPIENT'S CATALOG NUMBER
4. TITLE (and Subtitle) SHOCK INDUCED STARTING OF GASDYNAMIC LASER NOZZLES		5. TYPE OF REPORT & PERIOD COVERED Master's Thesis
7. AUTHOR(s) Paul A. Weber Captain USAF		6. PERFORMING ORG. REPORT NUMBER
9. PERFORMING ORGANIZATION NAME AND ADDRESS Air Force Institute of Technology (AFIT/EN) Wright-Patterson AFB OH 45433		8. CONTRACT OR GRANT NUMBER(s)
11. CONTROLLING OFFICE NAME AND ADDRESS Air Force Institute of Technology (AFIT/EN) Wright-Patterson AFB OH 45433		10. PROGRAM ELEMENT, PROJECT, TASK AREA & WORK UNIT NUMBERS
14. MONITORING AGENCY NAME & ADDRESS (if different from Controlling Office)		12. REPORT DATE December 1979
		13. NUMBER OF PAGES 101
		15. SECURITY CLASS. (of this report) UNCLASSIFIED
		15a. DECLASSIFICATION/DOWNGRADING SCHEDULE
16. DISTRIBUTION STATEMENT (of this Report) Approved for public release; distribution unlimited.		
17. DISTRIBUTION STATEMENT (of the abstract entered in Block 20, if different from Report)		
18. SUPPLEMENTARY NOTES Approved for public release; IAW AFR 190-17 JOSEPH P. HIPPS, Major, USAF Director of Information		
19. KEY WORDS (Continue on reverse side if necessary and identify by block number) Shock Tube Nozzle Starting Laser Nozzles Gasdynamic Laser Supersonic Nozzle Shock Tube Instrumentation Shock Propagation Time Delay Computer		
20. ABSTRACT (Continue on reverse side if necessary and identify by block number) Dynamic processes occurring in single and multiple arrays of contoured Mach 3.2 rapid expansion, two-dimensional, supersonic nozzles during the passage of strong shock waves were investigated. Two sizes of single throat nozzles were tested. Their throat openings were 0.276 and 0.069 inch. The multiple nozzle array used had nine parallel nozzles of the smaller size arranged to simulate the flow channel of a gasdynamic laser. Several series		

DD FORM 1 JAN 73 1473

EDITION OF 1 NOV 65 IS OBSOLETE

UNCLASSIFIED

SECURITY CLASSIFICATION OF THIS PAGE (When Data Entered)

UNCLASSIFIED

SECURITY CLASSIFICATION OF THIS PAGE(When Data Entered)

Block 20.

of schlieren photographs were taken of the flow field within the nozzles. A fully started condition evidenced by uniform supersonic flow was observed in the small single nozzle and the multiple throat array approximately 80 microseconds after the passage of Mach 2.33 shock waves. The large single nozzle was not fully started by Mach 3.0 incident shock. The dynamic flow initiation process was found to be strongly influenced by the strength and frequency of transverse wave reflections in the nozzle inlets. The large single nozzle's failure to start was found to be due to an unfavorable relationship between the frequency of these reflections and the time required for downstream dissipative processes to raise the expansion section static pressure to levels preventing supersonic flow initiation.

A novel digital time delay computer was designed and built to facilitate making closely spaced photographs of the flow patterns. This device makes shock location in each photograph independent of the shock wave speed.

UNCLASSIFIED

SECURITY CLASSIFICATION OF THIS PAGE(When Data Entered)